A Model For The Absorption Of Thermal Radiation By Gold-Black

Brendan R. Quinlan

Thesis submitted to the faculty of the Virginia Polytechnic Institute and State University
in partial fulfillment of the requirements for the degree of

Master of Science
In
Mechanical Engineering

J. Robert Mahan, Chair
Brian Vick
Vinh Nguyen

September 25, 2015
Blacksburg, VA

Keywords: Gold-black, Fractal, Electrical Circuit, Thermal Radiation, Detection

A Model For The Absorption Of Thermal Radiation By Gold-Black

Brendan R. Quinlan

ABSTRACT

The work presented here addresses an important topic in thermal radiation detection when gold-black is used as an absorber. Sought is a model to simulate the absorption of thermal radiation by gold-black.

Fractal geometry is created to simulate the topology of gold-black. Then electrical circuits based on the topology are identified that capture the physics of the interaction between the gold-black material and incident electro-magnetic radiation. Parameters of the model are then adjusted so results obtained are comparable to absorption data from the literature.

Potential next-generation radiometric instruments will likely involve thermal radiation detectors using gold-black as an absorbing medium. A model that accurately simulates gold-black absorption will be an important tool in their design.

Acknowledgements

I would like to thank my advisor, Dr. J. R. Mahan, for giving me the opportunity to explore the exciting field of radiation heat transfer. Without Dr. Mahan's insight, patience, and support, this thesis would not have been possible.

I would also like to thank my committee members, Dr. Brian Vick and Dr. Vinh Nguyen, for serving on my committee and for their help and support.

I also wish to thank all of my friends at Virginia Tech for keeping me more or less sane. Special thanks to Gordon Christie for his Matlab expertise and to Eli Whipple.

Lastly I would like to thank my parents, Joe and Lisa for their love and support.

Contents

List of Figures

List of Tables

Nomenclature

English:

A	Cross-sectional area
a	Distance between conductors
B	Number of braches
C	Capacitance (F)
d	Diameter of one conductor
E	Expected value
$\vec{E}$	Electric field strength vector $\left(\frac{V}{m}\right)$
f	Frequency (Hz)
G	Generation limit
$\vec{H}$	Magnetic field strength vector $\left(\frac{A}{m}\right)$
h	Average generation height
I	Current (A)
L	Inductance (H)
l	Characteristic dimension
l_{br}	Average branch length
M	Multiplier
N	Number of nucleation sites
P	Power (W)
$\vec{P}$	Poynting vector

q	Electric charge (C)
R	Resistance (Ω)
R_x	Normally distributed random number along the x-axis
R_y	Normally distributed random number along the y-axis
R_z	Normally distributed random number along the z-axis
S	Starting branch length
t	Time (s)
V	Electrical potential magnitude (V)
v	Sinusoidal electrical potential (V)
X	Reactance
x	Coordinate on the x-axis
y	Coordinate on the y-axis
Z	Impedance (Ω)
z	Coordinate on the z-axis

Greek:

α	Absorptivity
γ	Decay rate constant
θ	Average branching angle (deg)
λ	Wavelength (μm)
μ	Statistical mean
ρ	Reflectivity
σ	Standard deviation

ω	Angular frequency $\left(\frac{rad}{s}\right)$

Subscripts:

0	Quantity in vacuum
abs	Absorbed
g	Given generation
in	Incident
L	Inductor
R	Resistor
ref	reflected
rep	reported
res	Resonant
$total$	Totaled for all generations
x, y	x or y coordinate
λ	Given wavelength

Superscripts:

g	Given generation
ϕ	Phase angle

Constants:

c_0	Speed of light in a vacuum, $2.997925 \times 10^8 \frac{m}{s}$

j	Imaginary number operator, $\sqrt{-1}$
r_{gold}	Electric resistivity of gold, $2.44 \times 10^{-8}\ \Omega \cdot m$
ϵ_0	Permittivity of free space, $8.854 \times 10^{-12}\ \frac{F}{m}$
μ_0	Permeability of free space, $4\pi \times 10^{-8}\ \frac{N}{A^2}$

Chapter 1: Introduction

1.1 Objective

An emerging technology for space applications, called gold-black, has been used in thermal radiation detectors on current instruments and is being considered for future instruments intended to monitor the Earth's radiation budget. One possibility for thermal radiation detection is a micro-bolometer, which consists of several layers of insulating and electrically conducting materials with gold-black deposited on the upper surface, as described by Wang and Zhao [2012] and illustrated in Figure 1.1. A micro-bolometer operates by converting thermal radiation into heat. The heat changes the electrical resistance of a sensitive layer. The difference in electrical resistance is interpreted in terms of the absorption of thermal radiation. Modeling the absorptance of thermal radiation by gold-black is an area of intense research and development. This thesis represents an attempt to create a theoretical model for describing the absorptance of thermal radiation by gold-black.

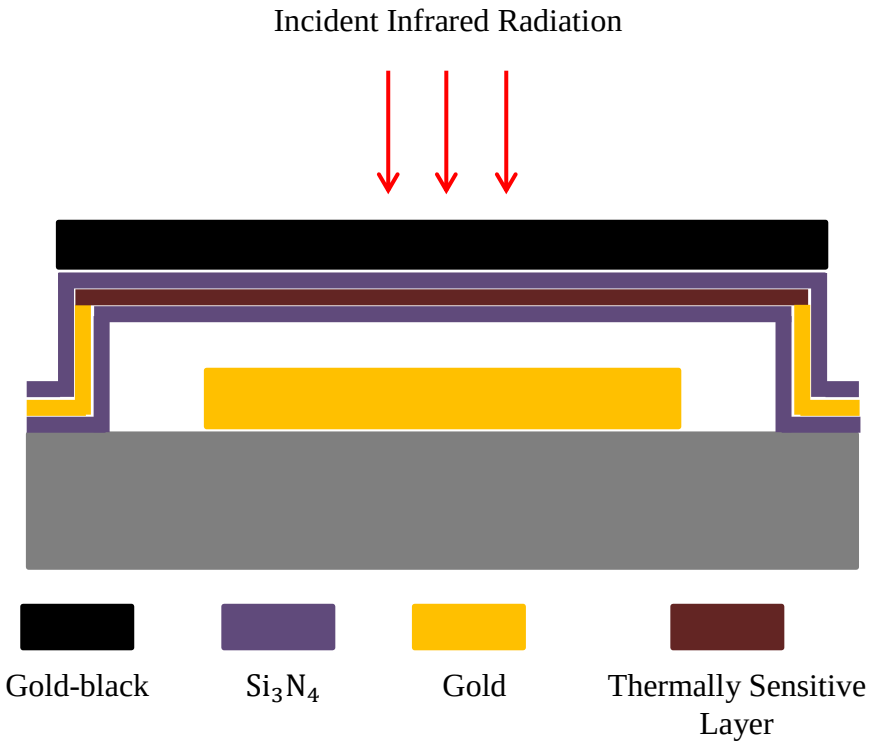

Figure 1.1: Schematic diagram of a micro-bolometer.

1.2 Current and Future Gold-Black Applications

For several decades NASA has been monitoring the Earth's radiation budget using instruments embarked on satellites designed to detect thermal radiation. The latest such instrument is called the Clouds and the Earth's Radiant Energy System (CERES). CERES first flew in 1998 on board the Tropical Rainfall Measuring Mission (TRMM) observatory [NASA, 2015]. The goal of CERES is to monitor the Earth's radiation budget over an extended period of time in order to understand climate evolution. The CERES instrument suite consists of three thermistor bolometer radiometers [Priestley, 1997]. Thermal models and rigorous testing are required in order to accurately determine the amount of radiation falling on a thermistor bolometer.

The European Space Agency's future counterpart to NASA's CERES program is called the EarthCARE broadband radiometer. The EarthCARE broadband radiometer attempts to monitor the Earth's radiation budget in a manner similar to that of CERES. However, EarthCARE will make use of an array of micro-bolometers with gold-black as an absorbing layer for thermal radiation [Proulx and Allard, 2010].

In order to apply new technologies to space applications, a certain level of maturity must be demonstrated. The maturity of gold-black will be advanced by the emergence of a reliable and accurate theoretical model.

1.3 Motivation for Research

During the past year, the Thermal Radiation Group (TRG) at Virginia Polytechnic Institute and State University, under the direction of Professor J.R. Mahan, has been collaborating with scientists and engineers at NASA's Langley Research Center to better understand and characterize emerging space-based radiometry intended for use in monitoring the Earth's radiation budget. The Earth's radiation budget refers to the balance between the incident thermal radiation from the sun and the outgoing reflected solar radiation and thermal radiation emitted by the Earth, as illustrated in Figure 1.2.

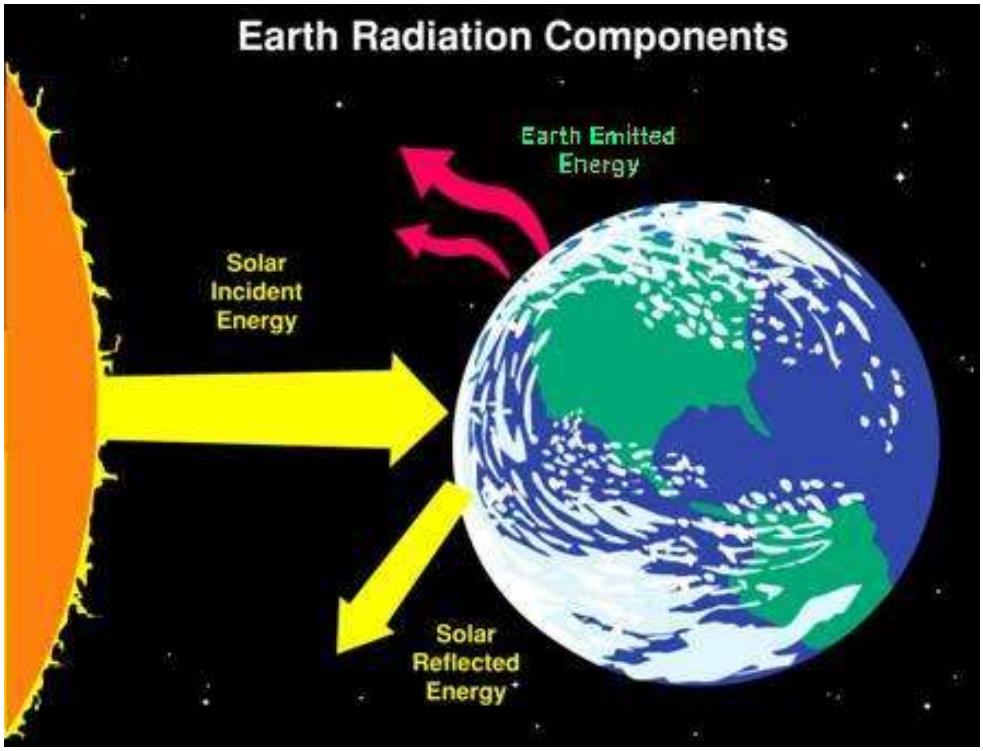

Figure 1.2: The Earth's radiation budget [NASA, 2011, What is the Earth's Radiation Budget?, http://science-edu.larc.nasa.gov/EDDOCS/whatis.html] Used under fair use, 2015.

A theoretical model of gold-black will enhance the ability of scientists and engineers to design thermal radiation detectors. Specifically, such a theoretical model will permit engineers to predict the behavior of absorbing layers, thereby enabling them to optimize the performance of any new gold-black-based thermal radiation detector concept.

1.4 Thesis Preview

The following procedure has been followed to produce a theoretical model for gold-black absorption. First, salt crystals were grown to gain insight into growth patterns and dependencies on physical conditions. Similarities are established between the growth of salt crystals and the deposition of gold-black based on reports in the literature and observations by the author. Dependence of salt crystal growth on physical conditions is implied based on these observations. A set of rules emerges governing the simulated growth of gold-black.

Next, principles of fractal geometry are applied to simulate the physical structure of a gold-black deposit. Patterns are then recognized in the fractal geometry which are the basis for implying a collection of electrical circuits. Finally, electro-magnetic radiation applied to the electrical circuits in the form of a simulated alternating-current potential difference. The subsequent conversion of EM energy into sensible heat through resistors represents the absorption of thermal radiation. Absorption as a function of wavelength of the incident radiation is then compared to experimental results from the literature. The process may be summarized as:

- Similarities between salt crystal growth and gold-black growth are observed.
- Relationships between salt crystal growth and physical conditions are postulated.
- Gold-black growth is simulated using fractal theory based on parameters identified by observing salt crystal growth.
- Electrical circuits are postulated as suggested by the simulated topology.
- Monochromatic absorption of thermal radiation is predicted based on the electrical circuit model.
- Theoretical and experimental absorption curves are compared in order to adjust parameters for acceptable agreement.

Figure 1.3 illustrates the iterative process described above used in this final step to develop the theoretical model discussed in the current effort.

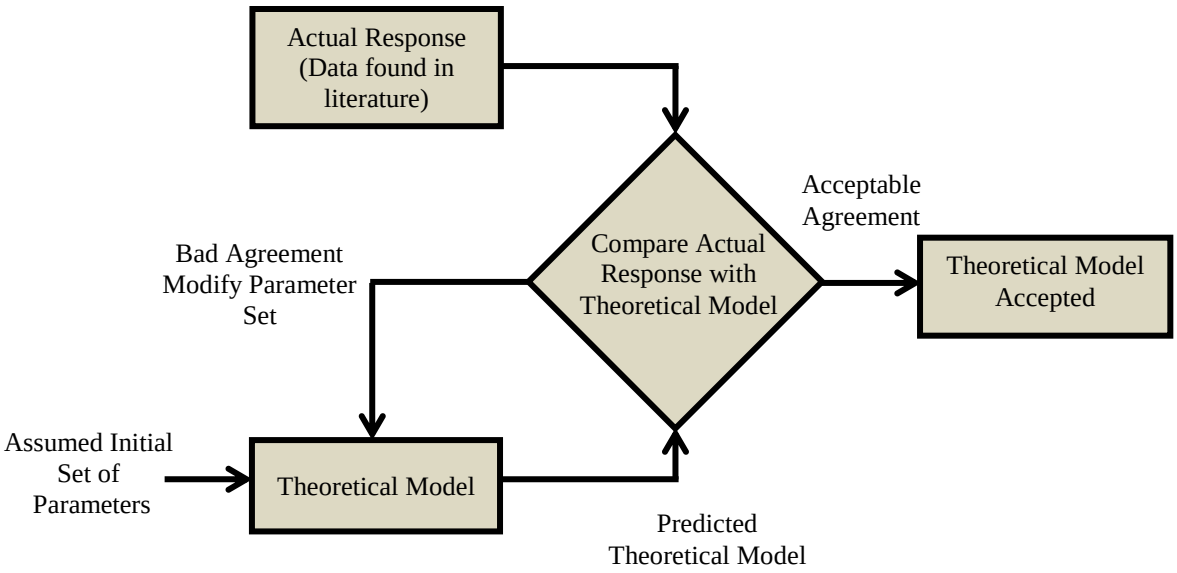

Figure 1.3: Block diagram for development of the theoretical model.

Chapter 2: Background

2.1 Gold-Black Description

According to Becker, *et al.* [1996] gold-black is a deposit of many microscopic "blobs" of sphere-like gold agglomerations that condense and deposit on a relatively cold surface. This process is similar to how frost layers or salt crystals accumulate on surfaces. By adjusting key factors, discussed elsewhere in this chapter, the buildup of microscopic sphere-like gold particles can be controlled to form a deposit of gold-black. The behavior of gold-black deposits when exposed to thermal radiation depends on these key factors. A gold-black deposit is illustrated in Figure 2.1.

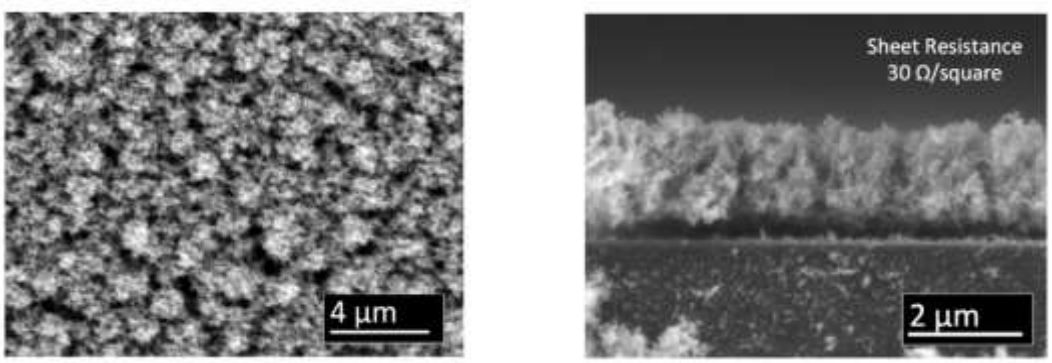

(a) (b)

Figure 2.1: Gold-black deposit, (a) plan view and (b) elevation view [Panjwani, Deep., Mehmet Yesiltas, Janardan Nath, D. E. Maukonen, Imen Rezadad, Evan M. Smith, R. E. Peale, Carol Hirschmugl, Julia Sedlmair, Ralf Wehlitz, Miriam Unger, Glenn Boreman, "Patterning of oxide-hardened gold-black by photolithography and metal lift-off" *Infrared Physics & Technology,* Vol. 62, pp. 94-99, 2014.] Used under fair use, 2015.

2.2 Gold-Black Production Process

The process described here has been in use since the 1930s. First reported by Pfund [1930], it was studied extensively in the 1950s by Harris and Cuff [1950] and Harris and Beasley [1952]. Even though the process described has been known for nearly 85 years, it is still used

today in the production and development of gold-black deposits [Nelms and Dowson, 2005]. However, gold-black has only recently begun to be exploited for thermal radiation absorption in space applications.

The general process for making a gold-black deposit starts with a vacuum chamber, as shown in Figure 2.2. The vacuum chamber may be fabricated from any material suitable for holding a vacuum and obtaining a low leak rate [Nelms and Dowson, 2005]. Two examples of vacuum chamber materials are stainless steel [Nelms and Dowson, 2005] and glass [Pfund, 1930].

Once the vacuum chamber has been fabricated, a pure nitrogen atmosphere is introduced to purge contaminates such as oxygen that may be present [Nelms and Dowson, 2005]. A pure nitrogen atmosphere is established by evacuating the vacuum chamber to the lowest pressure achievable with the pumps available. Pure nitrogen is then allowed to enter the chamber until the desired pressure is attained. A tungsten filament, discussed later, is then heated to remove any remaining oxygen [Nelms and Dowson, 2005]. At this point an appropriate atmosphere for a gold-black deposit has been achieved. The process temperature can be controlled by circulating nitrogen through the vacuum chamber or by forced convection cooling of the exterior surface of the vacuum chamber.

The tungsten filament used to further purify the nitrogen atmosphere also heats and melts a gold wire, as illustrated in Figure 2.2. The tungsten filament, which is heated electrically, may be in the shape of a V with a gold drop in suspension, as described by Harris and Beasley [1952] and McKenzie [1976]; a basket with a liquid gold pool, as described by Neli, *et al.* [2006]; or other configurations not specifically mentioned in the literature. The configuration of the tungsten filament is important in determining the evaporation rate and deposition rate of the gold

and has been a subject of extensive study. Tungsten is a common choice for a filament; however, other materials can be used. One other material, aluminum-oxide-coated molybdenum, was used by Nelms and Dowson [2005].

The gold filament, which is usually a wire, is made out of gold whose purity exceeds 99.99 percent [Nelms and Dowson, 2005]. Once a nitrogen atmosphere has been established at the appropriate pressure, the gold wire is electrically heated and melted. Then the gold is then evaporated by controlling the chamber temperature and pressure along with the electrical power to the tungsten filament.

Once the appropriate gold evaporation rate has been attained, the gold-black deposit surface is cooled by a cooling plate, as illustrated in Figure 2.2. The function of the cooling plate is to reduce the temperature of the gold-black deposit surface sufficiently to induce the buildup of a gold-black deposit through condensation [Nelms and Dowson, 2005].

The gold-black deposit surface shown in Figure 2.2 can be any material. However, it is typically material that is convenient for optical testing and/or easy to integrate into an electrical circuit; i.e., a metal or metal-impregnated weave.

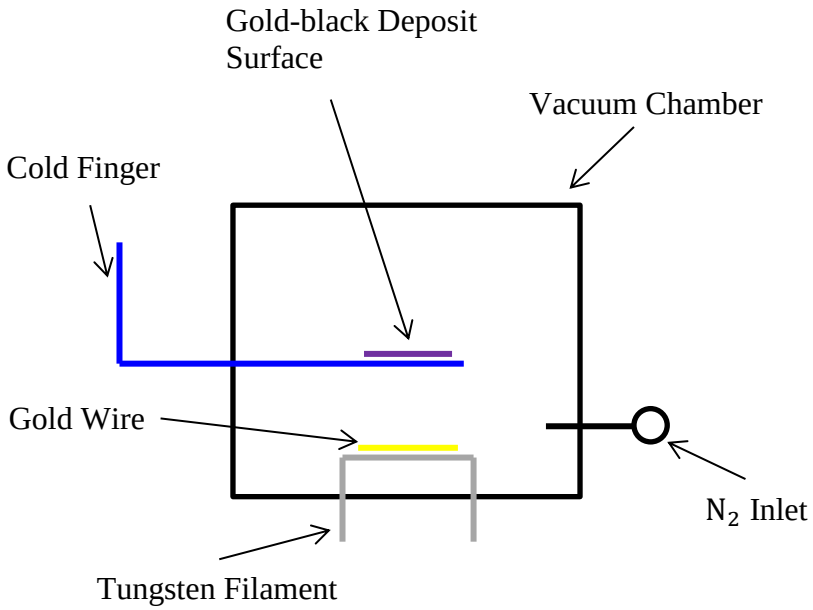

Figure 2.2: Schematic diagram of gold-black deposition process.

2.3 Gold-Black Absorptivity

In the literature many authorities promote gold-black as an excellent thermal radiation absorber. Three sources in particular; Nelms and Dowson [2005], Becker, *et al.* [1999], and Ilisa, *et al.* [2010]; vaunt gold-black as having an excellent absorptivity of thermal radiation over a wide wavelength range.

In general, gold-black is a very good absorber of visible light and near-infrared thermal radiation. Testing done by Harris and Cuff [1956] shows that one particular gold-black deposit has a total reflectance of less than or equal to one percent in the wavelength range of 0.400 to 1.100 μm. In the absence of significant transmittance through the underlying substrate, the absorptance of gold-black may be assumed close to unity.

Testing conducted by Nelms and Dowson [2005], Becker, *et al.* [1999], and Ilisa, *et al.* [2010] shows absorption or reflection for thermal radiation in the range of 0.2 to 100 μm. The absorptance characteristics of gold-black deposits appear to be determined by three main

conditions of the deposition process: chamber pressure, substrate temperature, and evaporation rate [Nelms and Dowson, 2005].

The chamber pressure is a critical factor in determining the deposition rate and density of a gold-black deposit. All pressures for forming a gold-black deposit are very low compared to atmospheric pressure. Typically the pressure in the vacuum chamber is adjusted between 1 and 15 mbar to produce gold-black deposits of different densities and thicknesses [Becker, *et al.,* 1999]. Gold-black deposits of different densities and thicknesses interact with thermal radiation differently. This is the result of the shape and size distributions and spacing of the actual gold particles. Different gold particle sizes and shapes interact differently with neighboring gold particles [Becker, *et al.,* 1999]. Also, the pressure determines how dense or closely packed the gold particles are, with a lower pressure resulting in a lower density and a higher pressure resulting in a higher density [Neli, *et al.*, 2006].

The temperatures of the atmosphere and the cooling plate during deposition are both critical factors in determining gold-black absorption characteristics. The temperature directly affects the deposition rate and the gold particle size distribution. As the gold is evaporated, the gold particles that agglomerate collide and form larger gold particles. Once the gold particles combine to a certain size, the energy in the atmosphere near the cooling plate will not be sufficient to maintain the gold atoms in vapor form [Becker, *et al.,* 1999].

The third critical factor in determining gold-black absorption characteristics is evaporation rate. The evaporation rate determines the number density of gold atoms in the vacuum chamber atmosphere at any moment. A low evaporation rate leads to low concentrations of gold vapor in the atmosphere, and the opposite is true for a high evaporation

rate [Harris and Beasley, 1952]. The evaporation rate is in turn controlled by electrical resistance heating of the tungsten filament.

Reflectance measurements reported by Becker, *et al.* [1999] for various materials are shown in Figure 2.3. The material labeled W44 is a gold-black deposit produced in a nitrogen atmosphere at a pressure of 8 mbar. The process used to create the gold-black deposit is similar to the one described above. For wavenumbers between 100 and 600 cm^{-1}, corresponding respectively to wavelengths of 100 and 16.7 μm, it is shown that the gold-black deposit listed as W44 has a reflectivity of no more than 7.5 percent. (The conversion between wavelength and wavenumber is $\lambda = 10\,000/\mathrm{k}$, with k representing wavenumber in cm^{-1} and λ representing wavelength in μm.)

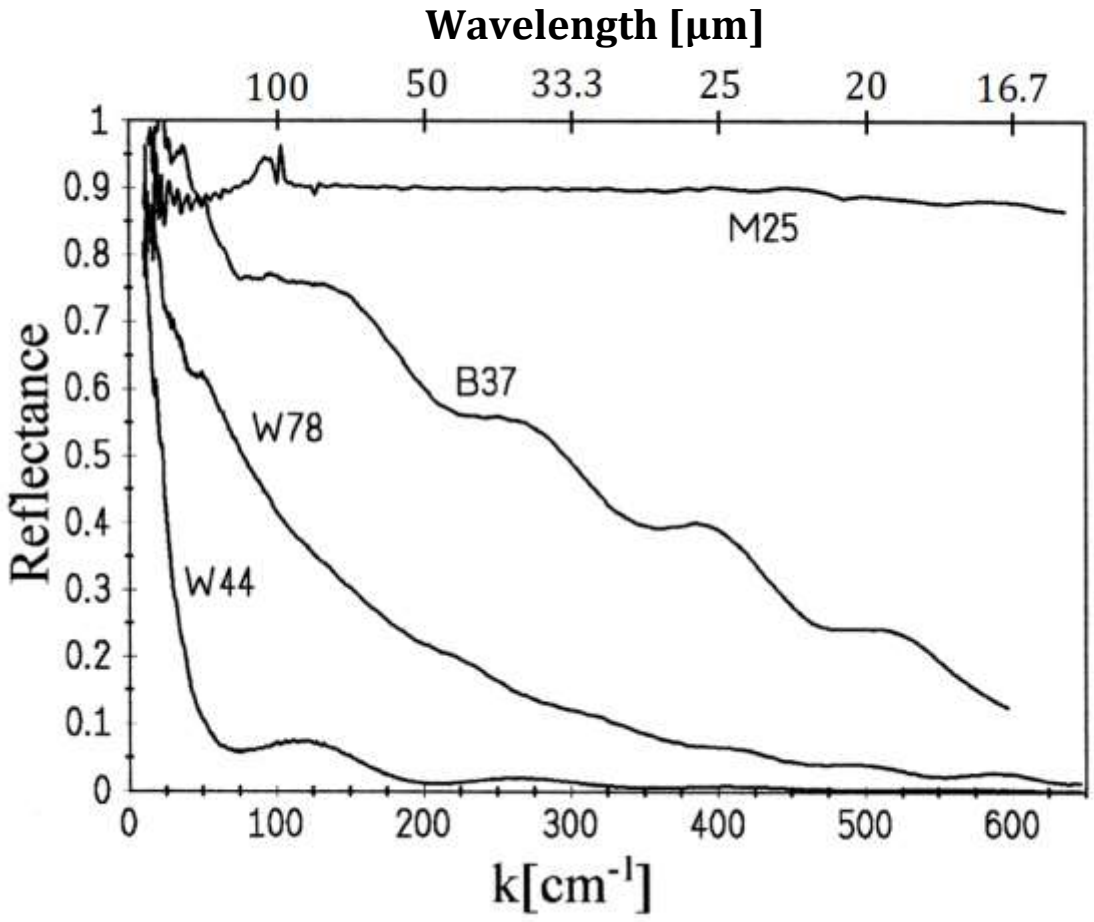

Figure 2.3: Specular reflectance as a function of wavenumber [Becker, W., R. Fettig, and W. Ruppel, "Optical and electrical properties of black gold layers in the far infrared" *Infrared Physics & Technolog.*, Vol. 40 pp. 431-445, April 1999.] Used under fair use, 2015.

The reflectance data shown in Figure 2.3 were obtained with a Fourier transform spectrometer. A mercury-arc lamp was used as a source of thermal radiation. According to Becker, *et al.* [1996], "All reflection measurements were made with a diffuse reflection unit where the averaged [zenith] angle of incidence φ varied between 30° and 50°". The specular reflection was then calculated as the ratio of the diffuse reflection to the reflection of a gold mirror.

The reflectance associated with the gold-black deposit W44 appears to vary little between 600 and 450 cm^{-1}. Beyond a wavenumber of 450 cm^{-1}, a series of undulations can be observed with increasing amplitude as wavenumber decreases (or wavelength increases). This pattern could be associated with interference as suggested by [Becker, *et al.*, 1999]. If so, this interference at the upper surface would result from radiation reflected from the substrate at the same wavelength but arriving with a different phase angle, thus resulting in constructive or destructive interference depending on the phase angle.

Ilias, *et al.* [2010] obtained reflectance measurements for a 6-deg angle of incidence from 0.2 to 100 μm, as illustrated in Figure 2.4. The maximum reflectance is estimated to be 7.5 percent. This implies very good absorption over a wide range of wavelengths. A nitrogen atmosphere with a pressure of 1.00 to 10.00 mbar was used to produce the gold-black deposit.

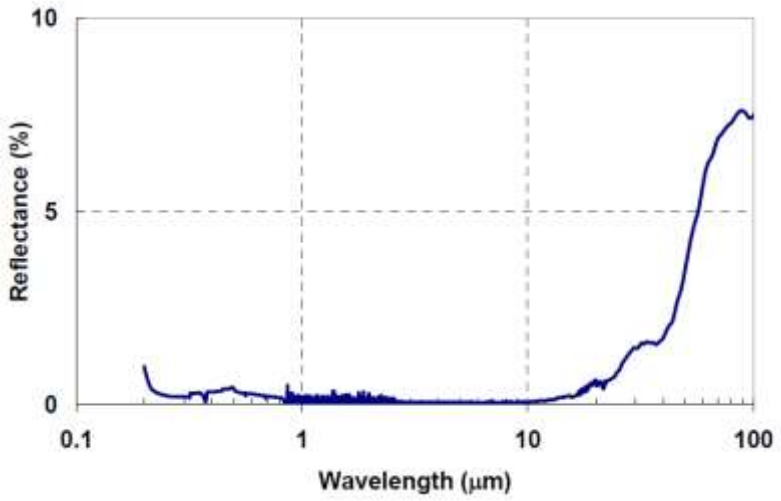

Figure 2.4: Specular reflectance of gold-black as a function of wavelength for a 6-deg angle of incidence [Ilias, S., P. Topart, C. Larouche, P. Beaupré, D. Gay, C. Proulx, T. Pope, C. Alain "Deposition and Characterization of gold-black coatings for thermal infrared detectors" *SPIE,* Vol. 7750, 2010.] Used under fair use, 2015.

The reflectance shown in Figure 2.4 was measured with two different spectrometers to cover the entire wavelength range shown. A Perkin-Elmer spectrometer with a parallel-beam

specular reflectance accessory was used to gather measurements from 0.2 to 2.5 μm, and a Bruker Vertex 70 spectrometer with various beam splitters and detectors was used to detect radiation in the far infrared range. Specular reflectance measurements were observed with these spectrometers. A highly polished pure gold substrate was observed as a reference. The absorption was determined by assuming the gold substrate to be "near unity over the whole wavelength of interest" and then subtracting the reflectance measurements from the gold substrate measurements [Ilias, *et al.,* 2010].

Nelms and Dowson [2005] report absorption as a function of wavelength ranging from about 2 to 40 μm, as shown in Figure 2.5. The three curves represent three different gold-black deposits that were produced under different conditions. The gold-black deposit with the best absorption, with an indicated deposition rate of 0.4 μg/s, was produced in a nitrogen atmosphere at a pressure of 10 mbar. Figure 2.5 indicates that gold-black has a specular absorption of greater than or equal to 90 percent for the entire range observed.

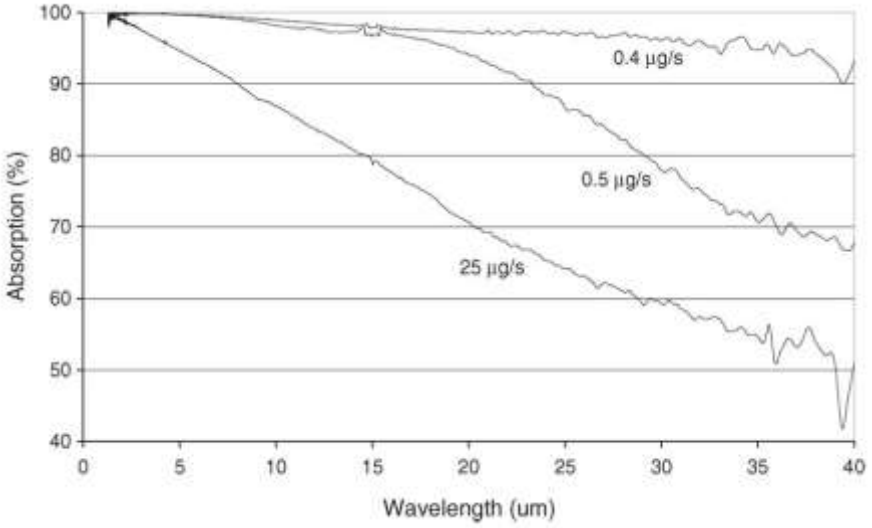

Figure 2.5: Specular absorption of three gold-black samples as a function of wavelength [Nelms, N. and J. Dowson, "Goldblack coating for thermal infrared detectors" *Sensors and Actuators A,* Vol. 120, pp. 403-407, Jan 2005.] Used under fair use, 2015.

The absorption data shown in Figure 2.5 were obtained with reflectance measurements from a Perkin-Elmer Spectrum with CsI optics and Specac diffuse reflectance accessory [Nelms and Dowson, 2005]. Gold-black deposits were prepared on top of a glass substrate with a layer of chromium followed by a layer of pure gold. A separate sample composed of a glass substrate with a layer of chromium followed by a layer of pure gold was used as a reference. Opacity of 100 percent was assumed for the reference sample. Assuming unity reflectance for specular gold, the absorption data were obtained by subtracting the reflectance measured from unity.

In summary, absorptance of gold-black deposits reported in Nelms and Dowson [2005], Becker, *et al.* [1999], and Ilisa, *et al.* [2010] is very high in the visible and infrared part of the electromagnetic spectrum. As has already been stated, the absorptance properties of gold-black are apparently affected by three main manufacturing variables: pressure, temperature, and evaporation rate. In general the high absorption rates are a result of the porous structure, which leads to a small heat capacity [Becker, *et al.*, 1999].

2.4 Previous Theoretical Models for Gold-Black

A theoretical model of gold-black absorption would be a useful tool in the development of a sensor to detect thermal radiation for the next-generation Earth radiation budget instrument. Harris and Beasley [1952] and Becker, *et al.* [1999] present theoretical models that predict gold-black absorption and reflection characteristics. Both of these models assume a homogenous medium and are based on the Drude model of free electrons, and both depend on optical observations made with a microscope to determine fitting parameters. As an alternative, the current author proposes a theoretical model based on the actual non-homogeneous topography in which small clusters or loops of two or more gold-black agglomerates generated by fractal geometry are interpreted as simple LRC electrical circuits. The introduction of a non-

homogeneous topography has the potential to create a model with a more realistic geometry than in the cited literature.

In the 1950s Harris and Beasley did extensive testing with gold-black to experimentally and theoretically determine gold-black absorption properties and curves. The theoretical models that resulted are based on assuming gold-black as a homogenous medium with a sea of free electrons. The equations found in Harris and Beasley [1952] are based on classical electromagnetic theory with a complex number representing the index of refraction, as in the Drude model of free electrons. The index of refraction was obtained assuming the electric permittivity and the magnetic permeability to be that of free space and used to calculate reflectance and transmission using equations derived from Stratton [1941].

Becker, *et al.* [1999] used a method similar to that of Harris and Beasley. They also used the Drude model of free electrons; however, approximations for the dielectric constant and the electrical conductivity for a two-component homogeneous medium were determined using optically observed fitting parameters. Fitting parameters were also used to match the theoretical behavior to the experimentally observed behavior.

2.5 Fractal Geometry

A fractal is an intricate geometric shape in which replicates of itself are repeated at arbitrarily small scales. The repetition is known as self-similarity. This means that if a small part of the overall shape is magnified the features are either identical or reminiscent of the whole. Many everyday objects can be described by fractals. For example the outline of clouds, electroplated surfaces, trees in a forest, and the cauliflower [Strogatz 2015, Schroeder 1991, and Mandelbrot 1983]. Based on observations and the literature presented in this chapter, the author of the present work has concluded that gold-black deposits can also be described as a fractal.

One of the earliest fractals discovered is known as the Cantor set. The Cantor set was introduced by Georg Cantor in 1883. The Cantor set starts out as a line. The line is replicated and moved down onto the next position under the starting line. The new line is divided into three equal sections with the middle section being removed. This set of instructions may be continued for any number of lines. Four iterations of the Cantor set are illustrated in Figure 2.6.

Figure 2.6: Illustration of the Cantor set with four iterations.

The Cantor set is an example of a fractal showing self-similarity in that the divisions resemble the starting condition when magnified appropriately. The Cantor set also exhibits a complex pattern as a whole that was derived from a very simple set of recursive instructions. The Cantor set theoretically continues for an infinite number of iterations; however, it must eventually terminate due to human fatigue or computer memory limits. When Georg Cantor introduced the Cantor set, the word "fractal" had not yet been coined, so infinitely recursive sets like the Cantor set were commonly known as "monsters" [Peitgen, *et al.*, 2004].

The relationship between fractal geometry and natural geometry was brought to the forefront in modern mathematics by the emergence of the digital computer. Mandelbrot accidently discovered fractals while studying noise generated by electrical disturbances over

transmission lines for IBM [IBM, 2011]. Mandelbrot started to replicate on the computer some of the fractal geometry reported by previous researchers. He found with the aid of a computer that much more detail or many more iterations could be obtained [Mandelbrot, 1983]. He used the computer to model natural geometries such as the roughness of various surfaces like the coast of Britain as fractals. Mandelbrot also coined the term "fractal." Since the introduction of the digital computer to generate fractal geometry, many studies have modeled geometry found in nature as fractals.

One area where fractal geometry has been used is ultra-wideband antenna arrays [Gross, 2011]. Ultra-wideband antenna arrays are commonly found in devices like cellular phones due to their selectivity over a wide range of frequencies. Ultra-wideband antenna arrays, or fractal antennas, are created in the shape of a variety of types of fractal geometry. Two main types of fractal antenna may be identified: deterministic and random [Gross, 2011]. Deterministic fractal antennas are constructed of recursive sets of instructions that do not incorporate randomness, for example the Cantor set. These geometries are ideal for creating antennas tuned to a wide range of specific frequencies. However, deterministic fractal antennas are usually not reminiscent of natural geometry due to their perfect symmetry.

Random fractal antennas, on the other hand, are constructed of recursive sets with randomness. Random fractal antennas are difficult to work with due to the fact that randomness results in a unique geometry for each antenna created. One method to create an antenna representative of natural geometries is a fractal-random tree, as described by Gross [2011]. The fractal-random tree is a type of polyfractal geometry. An example of a fractal-random tree is illustrated in Figure 2.7.

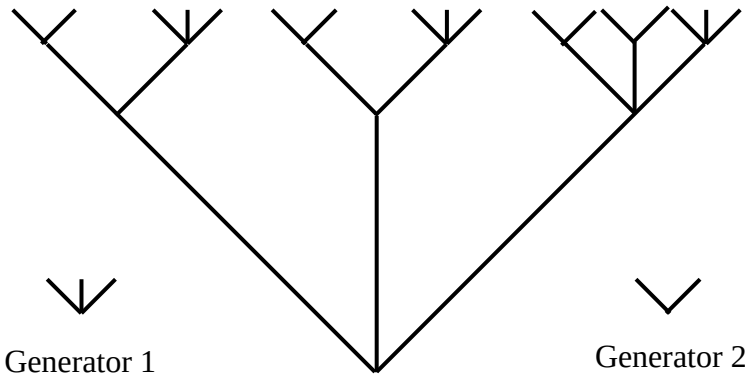

Figure 2.7: Fractal-random tree with two generators [Gross, Frank B., *Frontiers in Antennas: Next Generation Design & Engineering*, McGraw-Hill Book Company, Inc., New York, 2011.] Used under fair use, 2015.

An interesting characteristic of fractal antennas is that they usually do not need discrete components in order to resonate [Cohen, 1997]. The structure of the antenna itself is thought to act as discrete components. This makes fractal antennas cost effective when applied to small devices which need to resonate at many different frequencies.

Diffusion-Limited Aggregation (DLA) is a computer model developed to describe fractal growth driven by diffusion. Witten and Sander proposed the model in 1981 to describe natural phenomenon consisting of aggregates, such as gold-black, cab-o-sil, and coagulated aerosols, that are primarily driven by diffusion processes. Aggregates are clusters of particles that have accumulated due to Brownian motion. Brownian motion is the random motion of small particles suspended in a fluid provoked by collisions with atoms. The simulation of a fractal according to the DLA model presented by Witten and Sander starts at a central location. Random walks, which represent accumulating particles, are allowed to diffuse and cluster together to form an aggregate, as illustrated by Figure 2.8 taken from Witten and Sander [1981]. A random walk is a term used to define growth in random directions. It is described by Kaye [1994] as a drunk who

tries to stagger away from a lamp-post. As the drunk takes one step from the lamp-post he may stagger to the left and right and even backwards and forwards.

Figure 2.8: Random aggregate of 3600 particles on a square lattice [Witten, T. A and L. M. Sander, "Diffusion-Limited Aggregation, a Kinetic Critical Phenomenon" *The American Physical Society*, Vol 47 No 19, 1981.] Used under fair use, 2015.

Chen *et al.* [2013] describe simulating frost as a fractal. They used an optical camera to observed frost growing in a controlled environment. The frost layer observed was determined to grow according to the DLA model developed by Witten and Sander. Using the DLA model Chen and Yao successfully simulated frost growth which compared well with observations.

The present author, based on sources in the literature and his own observations reported in this effort, has concluded that gold-black growth is a fractal phenomenon. Simulating and

analyzing a gold-black structure based on fractal geometry promises to lead to more accurate models of gold-black absorption of thermal radiation.

2.6 Fractal Geometry as a Collection of Independent Electrical Circuits

Electrical circuits discussed in this section and in later chapters refer to circuits constructed of resistors (R), inductors (L), and capacitors (C) that are connected in series or parallel. An assembly of electrical circuits usually consists of hundreds if not thousands of connections. The types of connection and components (series/parallel and R, L, or C) may be determined by fractal geometry. The basic concept is to replace small sections or clusters of the fractal geometry with R, L, and/or C components. The branch points and connection points will determine whether circuit segments will be in series or parallel. The process is illustrated in Figure 2.9 for a circuit comprised of resistors only. The author believes that phenomena such as the absorption of thermal radiation by gold-black can be better understood by constructing electrical circuits from fractal geometry.

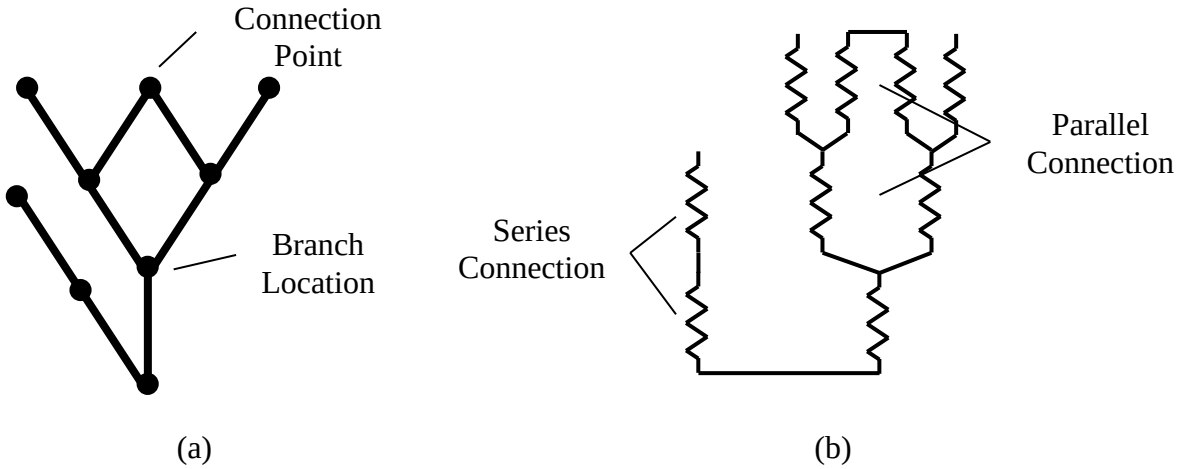

Figure 2.9: (a) Sample fractal geometry and (b) Electrical circuit replacing fractal geometry.

Another area where investigators have used the technique illustrated in Figure 2.9 is in the description of the interface between an electrode and an electrolyte in a battery. Such a

model has been reported by Liu [1984]. Liu describes the surface of an electrode as a fractal resembling the Cantor set, as illustrated in Figure 2.10 (a). The branches are replaced with electrical components to make a network of electrical circuits, as illustrated in Figure 2.10 (b).

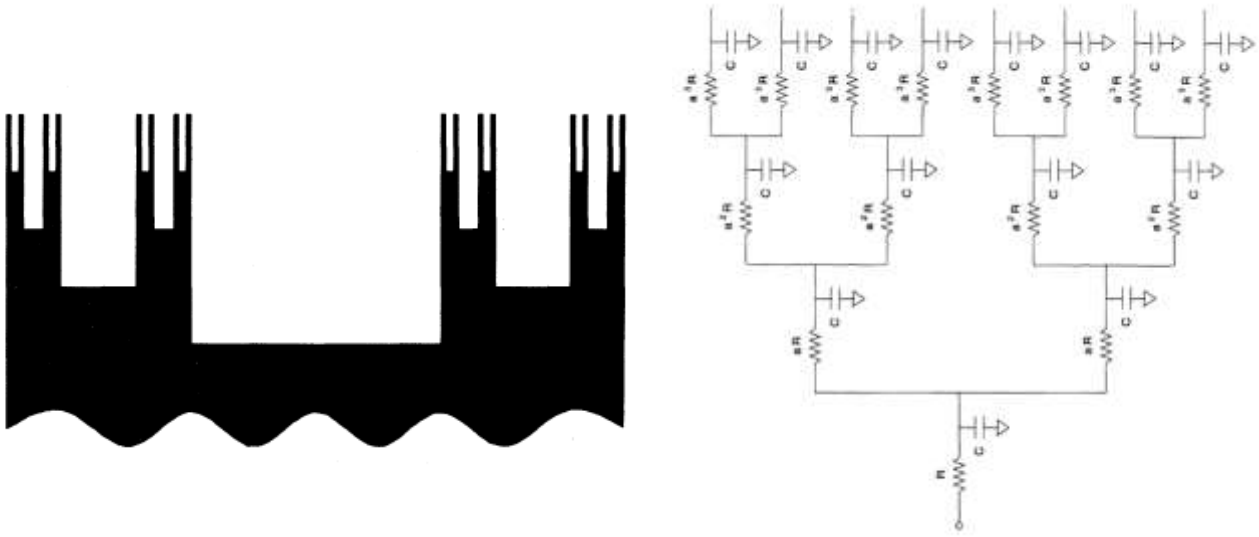

(a) (b)

Figure 2.10: (a) Fractal geometry representation of electrode surface, (b) Electrical circuits in place of fractal geometry [Liu, S. H., "Fractal Model for the ac Response of a Rough Interface", *The American Physical Society*, Vol. 55 No 5., 1984.] used under fair use, 2015.

This intuitive model is valuable for relating fractal geometry, which represents natural geometry such as gold-black, to natural phenomenon such as absorption of thermal radiation by gold-black. The present author believes that by creating a theoretical model according to the steps outlined in Section 1.4, more insight and a more accurate model will emerge compared to previous theoretical models such as those proposed by Harris and Beasley [1952] and Becker, *et al.* [1999], which assume a physically homogeneous medium.

Chapter 3: Salt Crystal Observations and Physical Relationships

3.1 Why Salt Crystals?

In order to correctly simulate the fractal geometry growth of gold-black, one must first observe the phenomenon. However, creation of a gold-black deposit requires a considerable investment of time and money. As described in Section 2.2, a vacuum chamber must be obtained and environmental factors such as temperature, pressure, and atmospheric conditions within the vacuum chamber must be controlled to a high degree of accuracy. The current effort to develop a theoretical model for gold-black was subject to limitations on time and money. According to Bunde [1991] studying fractal geometries made in a similar manner will lead to insights of general value. Therefore, under significant time restrictions and subject to a limited budget, the author has chosen to examine fractal geometry similar to gold-black.

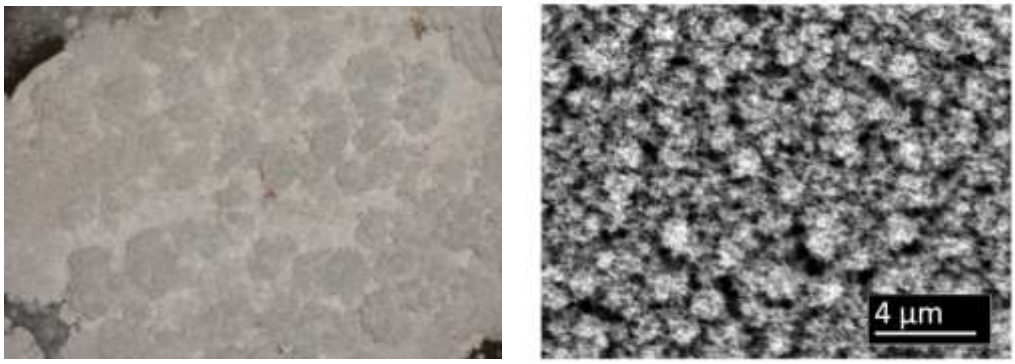

(a) (b)

Figure 3.1: (a) Plan view of salt crystals obtained by the author, and (b) Plan view of gold-black [Panjwani, Deep., Mehmet Yesiltas, Janardan Nath, D. E. Maukonen, Imen Rezadad, Evan M. Smith, R. E. Peale, Carol Hirschmugl, Julia Sedlmair, Ralf Wehlitz, Miriam Unger, Glenn Boreman, "Patterning of oxide-hardened gold-black by photolithography and metal lift-off" *Infrared Physics & Technology*, Vol. 62, pp. 94-99, 2014.] Used under fair use, 2015.

Salt crystals were chosen as an experimental medium in order to gain insight into the rules that govern growth characteristics. They can be grown with relative ease at atmospheric

pressure and at room temperature and appear remarkably similar to gold-black growth, as illustrated in Figure 3.1. The observations made by the author are translated to the gold-black growth simulation. The salt crystals observed by the author consist of a combination of two salt crystals as described by Katz [2005].

According to Katz, growth of the salt crystals is due to evaporation of the growing solution into the surrounding environment. The evaporation of the growing solution can be described by a diffusion process where the growing solution diffuses into the environment leaving behind salt crystals. Key questions can be posed and perhaps answered to generate a set of rules governing simulated gold-black growth by observing salt crystal growth. These questions may be stated

- How does the growth begin?
- How do the salt crystals grow; e.g., branching, DLA, percolation, etc.?
- How does late growth compare to early growth?
- Is the growth pattern self-similar?
- Do branches intersect, and if so how do they interact?

3.2 Salt Crystal Experimental Set-up and Procedure

The apparatus used to observe salt crystals is illustrated in Figure 3.2.

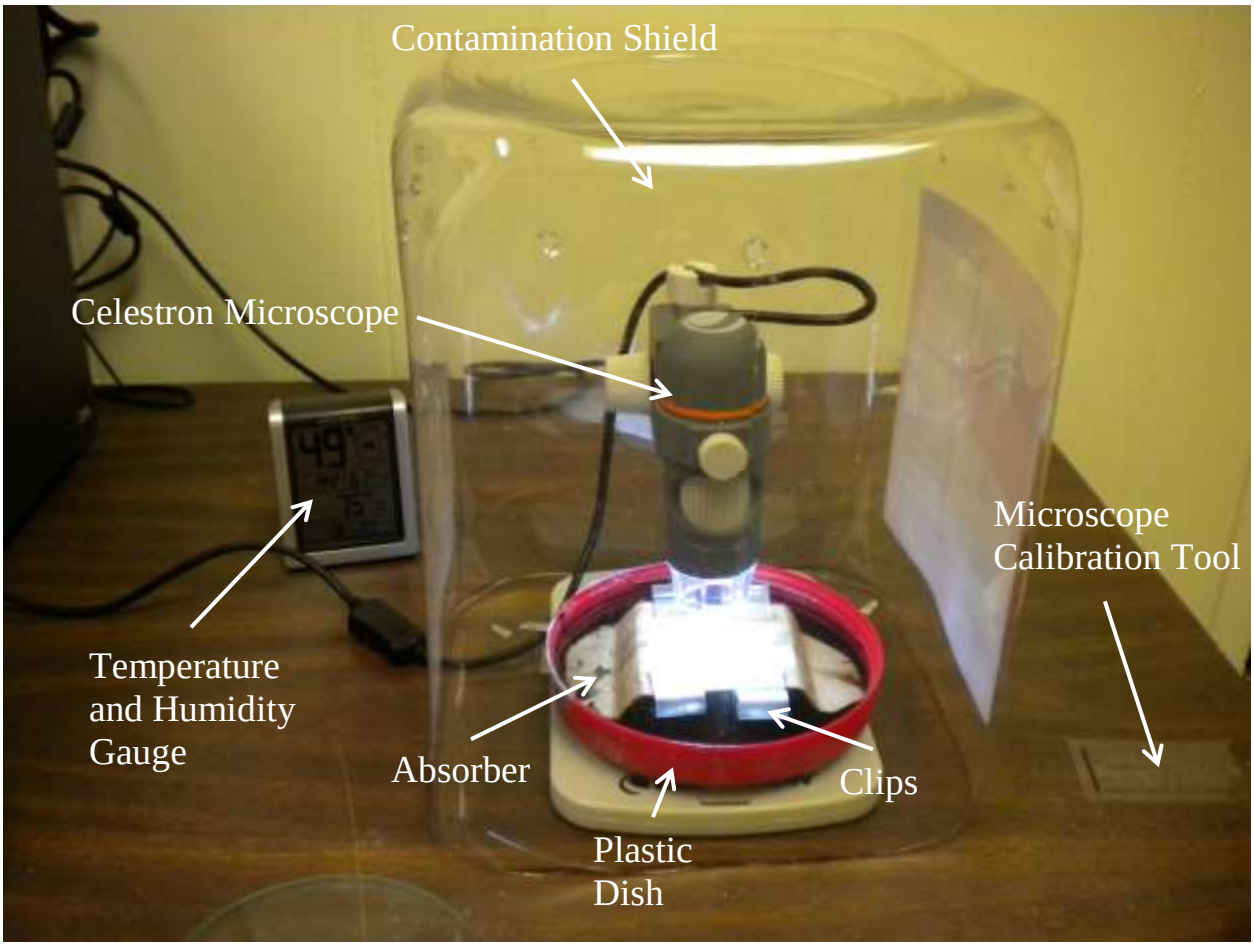

Figure 3.2: Apparatus used to observe salt crystals.

The growing solution is comprised of three components: household ammonia, Mrs. Stewart's® liquid bluing, and table salt. The growing solution is mixed together in the plastic dish with equal amounts of each component. The general growing solution formula comes from Jefco, Inc., the company that produced Mrs. Stewart's liquid bluing [Jefco, Inc.]. This process is also called a salt crystal garden and is in common use by hobbyists and artists.

The absorber substrate is fabricated from light cardboard, for example the cardboard used in the center of a roll of toilet paper. This material is shaped appropriately to fit the dish. The

purpose of the absorber substrate is to provide a surface for salt crystal growth and a porous medium through which the growing solution penetrates and spreads via capillary action.

The clips ensure that the absorber remains stationary and provides a relatively flat growing surface. The plastic dish is a common container lid and acts as a receptacle for the growing solution. The ambient temperature and humidity are monitored by using an AcuRite® temperature and humidity gauge positioned just outside the contamination shield.

The contamination shield is fabricated from a large animal crackers container. The contamination shield is constructed by cutting off the top of the container and piercing approximately ¼-in. holes in the bottom for ventilation purposes. The container is then inverted and placed over the dish, as illustrated in Figure 3.2. The contamination shield is required to shield the salt crystals from dust, insects, and air currents.

A Celestron® digital microscope is used to capture video and images at different magnifications. Finally, a microscope calibration tool, provided by Celestron, is used to determine the magnification of the microscope.

The procedure for growing salt crystals may be described as follows. The growing solution is created by mixing together in the plastic dish 1 tbsp. of each component: household ammonia, Mrs. Stewart's liquid bluing, and table salt. The absorber is placed in contact with the growing solution in the plastic dish, as shown in Figure 3.3. Clips are added to ensure a flat surface for salt crystal growth. The plastic dish is then placed under the microscope. The contamination shield is then placed over the microscope and plastic dish. The temperature and humidity gauge is placed next to the apparatus. The entire assembled apparatus is illustrated in Figure 3.2.

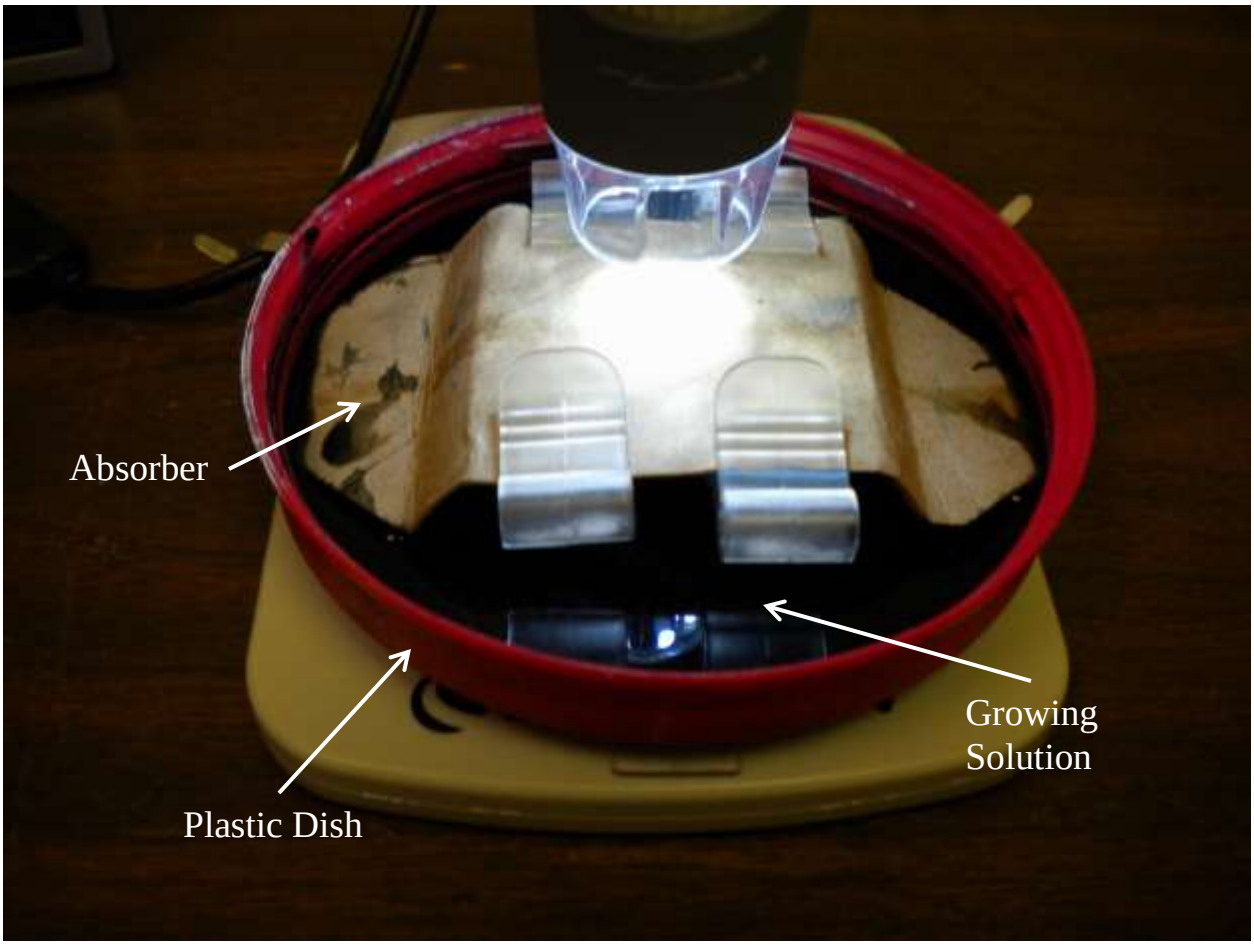

Figure 3.3: Assembled plastic dish, absorber, and growing solution.

The procedure for growing salt crystals may be summarized as follows:

- In the plastic dish, mix together 1 tbsp. of household ammonia, 1 tbsp. of Mrs. Stewart's liquid bluing, and 1 tbsp. of table salt.
- Set the absorber in the solution, as shown in Figure 3.3.
- Place the plastic dish under the Celestron microscope.
- Place the contamination shield over the Celestron microscope and the dish.
- Place the temperature and humidity gauge in the vicinity of the apparatus.
- Begin recording with the Celestron microscope.

3.3 Salt Crystal Observations

Nucleation sites begin to appear as the growing solution evaporates from the absorber. The nucleation sites, shown in Figure 3.4, consist of small white dots which are salt crystals left behind by the evaporating growing solution. The nucleation sites are apparently randomly distributed on the absorber.

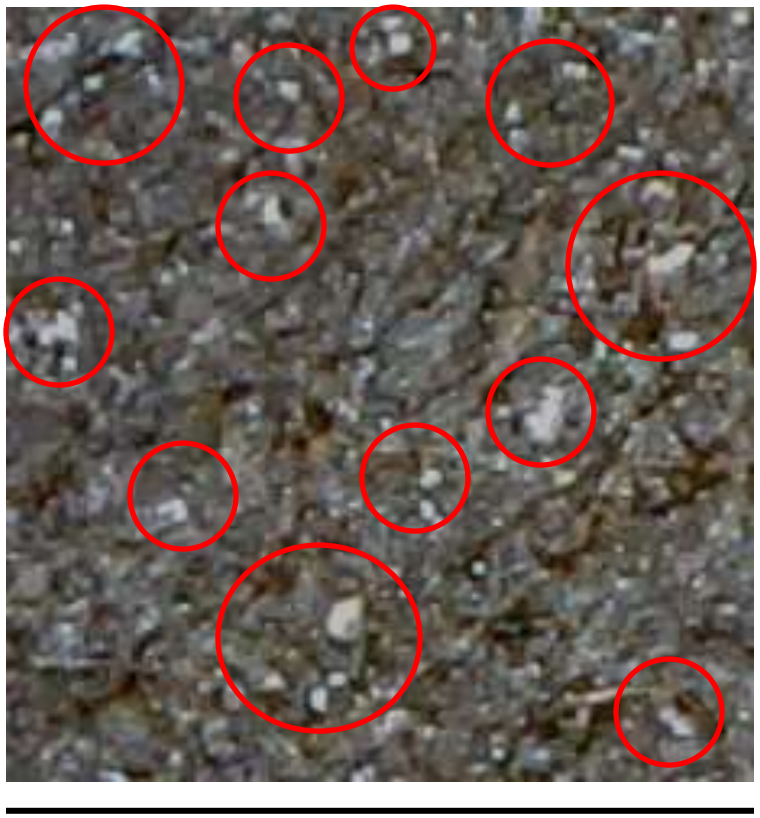

Figure 3.4: Formation of nucleation sites.

Two or three branches that propagate upwards from the nucleation site are prevalent with each generation of growth, as shown in Figures 3.5 and 3.6. The growth of all the branches shown in Figures 3.5 and 3.6 appear to be self-similar from generation to generation. The process does indeed appear to be driven by diffusion of the growing solution evaporating into air as described by Katz [2005]. The subsequent growth from the nucleation sites is similar to DLA

dendrite growth, as described in Section 2.4. However, the growth shown in Figures 3.5 and 3.6 does not exactly follow the definition of a random walker, as described in Section 2.5, but is instead a biased random growth that favors upward growth.

Figure 3.5: Observation of two-branch pattern at two moments in time.

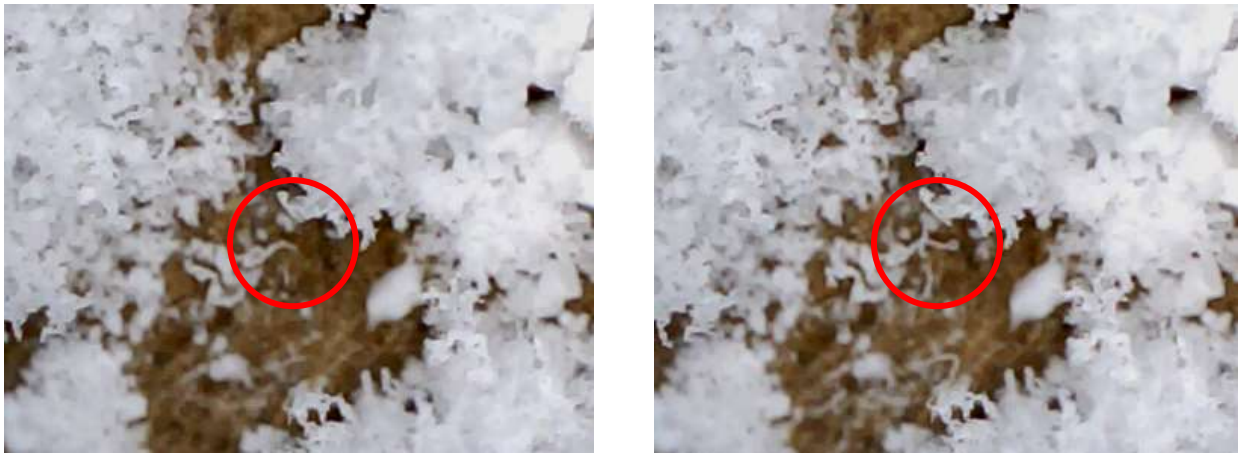

Figure 3.6: Observation of three-branch pattern at two moments in time.

The incidence of specific branch types in Figures 3.5 and 3.6 is limited because branches growing with an orientation observable by the microscope are relatively rare.

Salt crystals were observed to have a coarse structure initially while a fine structure emerges at the end of the growth cycle. The internal geometry was observed visually by the author and his advisor after a probe was used to remove part of the salt structure.

Figure 3.7 shows that some of the salt crystal branches join and form a connection. During the connecting process, two neighboring branches tend to join by melting together. When the connection occurs, the growth seems to be stunted at the connection site.

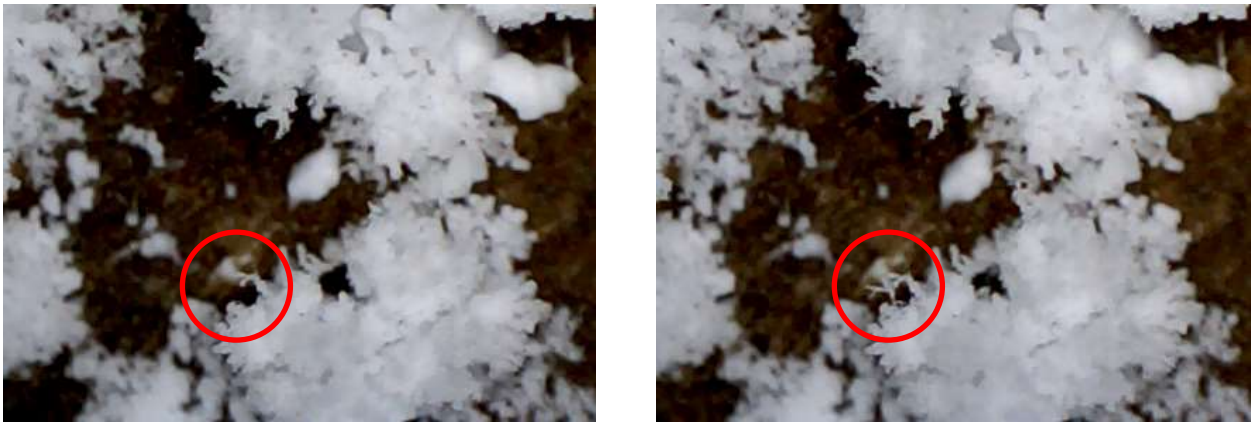

Figure 3.7: Observation of branches intersecting and connecting with each other.

The observations discussed provide answers to key questions that are exploited later in the simulation of gold-black growth. These observations and subsequent answers are very helpful in composing a growth simulation model that is representative of natural fractal geometry. The answers to the five questions posed on page 25 in Section 3.1 are the result of observations of salt crystals and may be summarized thusly:

- Growth begins with nucleation sites whose distribution appears to be random.
- Growth seems to be similar to a modified DLA dendrite growth with a two- or three-branch pattern.
- A coarse structure prevails in early growth while a fine structure prevails in late growth.
- The growth is self-similar with each generation reducing in branch length.

- As branches grow and intersect with each other they tend make a connection.

3.4 Relationships between Gold-Black Growth and Physical Conditions

In order to compare gold-black deposits described in the literature with the theoretical model presented in this work, relationships must be established between physical conditions used to create a gold-black deposit and the parameters used in a corresponding numerical model. The literature review in Chapter 2 reveals three physical conditions that govern the formation of a gold-black deposit: evaporation rate, pressure, and temperature.

Analysis by Becker *et al*, [1999] and Nelms and Dowson [2005] indicate that evaporation rate is one of the driving factors behind the eventual degree of compactness of a gold-black deposit. The compactness of simulated gold-black growth is determined by adjusting the quantity of nucleation sites. A high evaporation rate should lead to sparsely spaced nucleation sites while a low evaporation rate should lead to closely spaced nucleation sites.

Another influence of evaporation rate on a gold-black deposit is the average gold droplet size that forms the gold conglomerates. As the evaporation rate increases, the average size of gold droplets increases, according to Becker *et al*, [1999]. The author of the present effort suspects that the smallest conglomerate that can be formed is a single gold droplet, or building block, as illustrated in Figure 3.8. A conglomerate is composed of several or even many gold droplets, and the overall structure is composed of many conglomerates. This is one possible explanation for the limitation of the number of generations in gold-black growth.

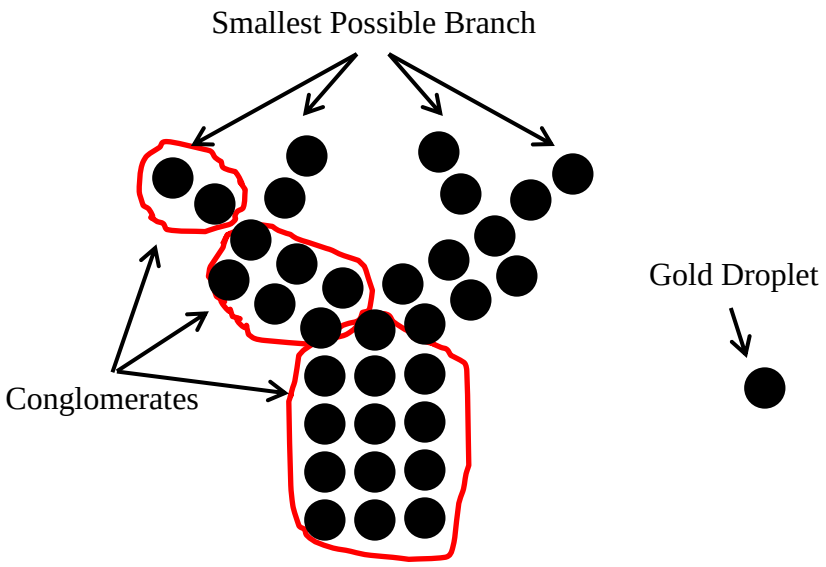

Figure 3.8: Illustration of smallest possible branch size limit.

Pressure is another factor, described by Becker *et al.* [1999], that influences the density of a gold-black deposit. As the pressure increases, the density of a gold-black deposit decreases and vice-versa [Neli, *et al.*, 2006]. The density refers to how much material is present per unit volume. This density may be related to branching from the nucleation sites. Compactness, on the other hand, describes how closely or sparsely the nucleation sites happen to form per unit surface area. The angle θ at which a branch diverges from the normal relates pressure to density in a gold-black simulation, as illustrated in Figure 3.9. If, for example, as the pressure increases the angle becomes larger and the density of the simulated gold-black growth would be reduced due to more connections between branches. Such connections terminate growth.

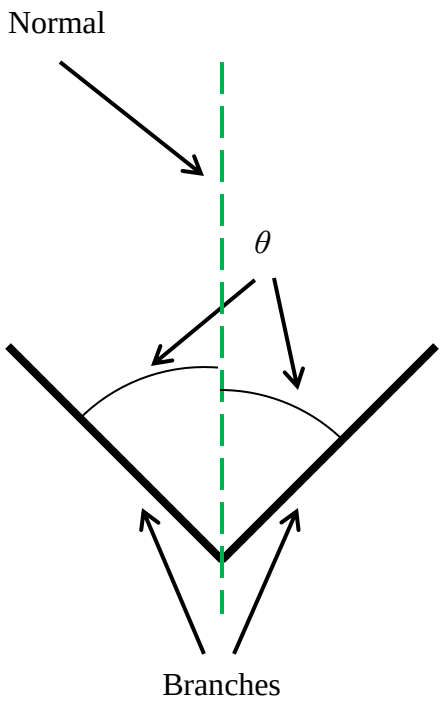

Figure 3.9: Branching angle illustration.

The last driving factor mentioned in the literature is temperature [Nelms and Dowson, 2005]. Specifically, the difference in temperature between the cold finger, shown in Figure 2.2, and atmospheric conditions within the chamber is key. The difference in temperature is represented in the present model by the rate at which subsequent branches reduce in length as compared to the length of the initial branch. The author of this work believes temperature influences gold-black growth in this way because, as the difference in temperature increases, longer initial branches can be formed due to more rapidly solidifying gold droplets.

The supposed relationships among physical conditions to create a gold-black deposit and the gold-black growth model presented here may be summarized as follows:

- A high evaporation rate leads to sparsely spaced nucleation sites, while a low evaporation rate leads to closely spaced nucleation sites.

- The number of generations decreases as evaporation rate increases due to increased gold droplet size.
- The density of a gold-black deposit decreases as the pressure increases resulting in larger branch angles.
- The difference in temperature between the cold finger and the chamber temperature is related to the rate at which subsequent branches reduce in length from generation to generation.

Chapter 4: Gold-Black Computer Simulation

4.1 Introduction to Simulating Gold-Black Deposition and Growth

A computer simulation has been created to represent the final structure resulting from growth of a gold-black deposit. The model is based on observations of salt crystals described in Section 3.3 and relationships between physical conditions and gold-black deposits described in the literature and discussed in Section 3.4. The overall structure of the program is based on observations from Section 3.3. Values of parameters used to match the gold-black computer simulation with gold-black deposits found in the literature were determined from the relationships drawn in Section 3.4. A detailed discussion of creating the computer simulation to model gold-black is provided in this chapter. The results are compared with images of actual gold-black deposits from the literature.

4.2 Gold-Black Simulation

A system of feedback loops must be implemented to simulate fractal geometry on a computer [Peitgen, *et al.,* 2004]. The resulting Matlab computer program is listed in Appendix A. Nucleation sites are created and produce two or three sets of coordinates corresponding to branches which extend and terminate for each generation. The coordinates of the branch terminations are then fed back into the program as starting points for a subsequent generation.

Independent branches intersect at connection points. As each branch is created, a function within the program determines if the newly created branch intersects with any surrounding branches and, if so, the newly created branch connects at that point and terminates. The point at which the newly created branch connects is a connection point as defined in Section 3.3. Branches in three dimensions can never really intersect with each other because a branch structure in which two branches pass through the same exact coordinates has a nearly zero

probability of occurring. In order to overcome this, any branch passing within one diameter of the branch being analyzed is identified and assumed to form a connection.

The program stores node locations in a queue. The queue concept is common in computer science applications. The data in the queue are processed by analyzing the nodes at the top of the queue and adding new nodes to the end of the queue. As nodes at the top of the queue are analyzed they are removed from the queue, and the new nodes created by analyzing the node at the top of the queue are then added to the end of the queue. The overall structure of the program is represented in block diagram form in Figure 4.1. Figure 4.2 shows elevation views on the left and oblique views on the right of a sample simulation depicting generation by generation growth using the computer program developed in this chapter.

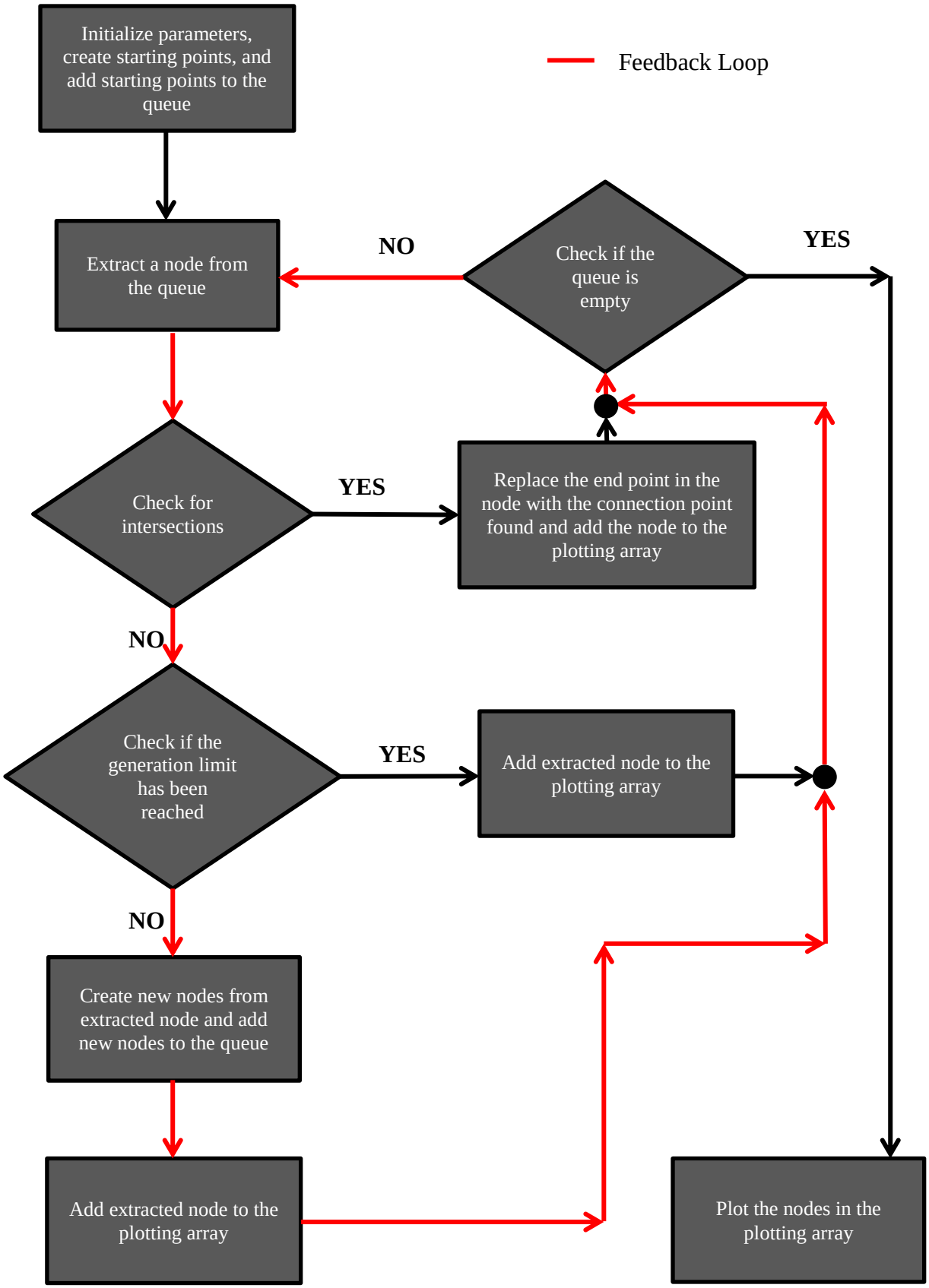

Figure 4.1: Block diagram of gold-black simulation.

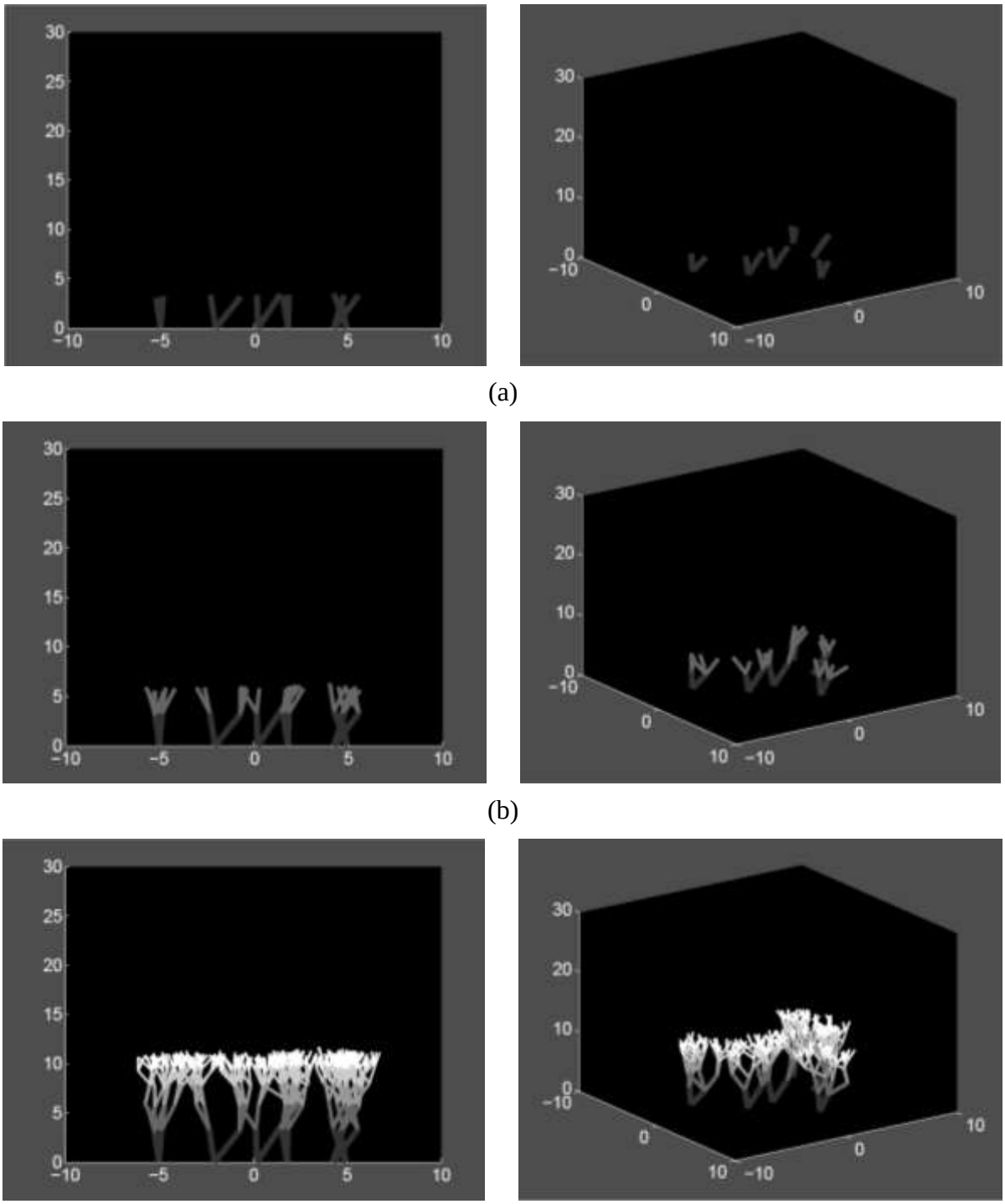

(a)

(b)

(c)

Figure 4.2: Generation by generation growth of gold-black simulation: (a) generation one, (b) generation two, (c) generation five.

Once the structure of the program has been established, the parameters identified in Section 3.4 can be incorporated. The specific techniques to incorporate these parameters are discussed in the following paragraphs.

The nucleation sites are supplied by generating random numbers and identifying them as the coordinates of the starting position of each branch. The nucleation sites are distributed randomly over an adjustable range in order to simulate compactness of the nucleation sites. The adjustable number of nucleation sites, denoted by N, represents the influence of evaporation rate on the simulated gold-black growth. A small number of nucleation sites will result in sparsely spaced nucleation sites, corresponding to a high evaporation rate, as stated in Section 3.4.

The number of generations created in the simulation is determined by a logical operator which stops growth at a predetermined value of a variable, denoted by G. The value of this predetermined variable represents the second influence of evaporation rate, as discussed in Section 3.4. A large number of generations created corresponds to a low evaporation rate, and a small number of generations created corresponds to a high evaporation rate.

The initial branch length and rate of branch length decay are both determined by the values of adjustable constants. The value of the initial branch length, denoted as S, is suggested by gold-black deposit thicknesses in the literature. A decrease in branch length from generation to generation is applied to create a self-similar geometry that decreases in length as generation number increases. This is accomplished by defining a constant number γ between zero and unity known as the branch decay rate constant. The branch decay rate constant is raised to the power corresponding to the generation number for each specific branch and multiplied with the coordinates of the branch being generated. Thus, if the branch decay rate constant is 0.9 for example, then the first generation would be 0.9^1 of the original and the second would be 0.9^2 of

the original generation, and so forth. Both constants are discussed in greater detail later. The initial branch size and the branch decay rate constant represent the influence of temperature on the gold-black simulation, as developed in Section 3.4. Values of γ near zero represent a low temperature difference and values near unity represent a high temperature difference.

Branching is accomplished by generating either two or three branches from each node created. This is implemented by generating a loop within the feedback cycle. A proportion of the number of two-branch divisions to three-branch divisions is assumed based on observations of salt crystal growth. The coordinate values are determined by the average branching angle, θ. The branching angle represents the influence of pressure, as discussed in Section 3.4. A large branching angle corresponds to a large standard deviation and leads to branches with larger angles, while a small branching angle corresponds to a small standard deviation and leads to more branches with smaller angles.

The author prescribes an average branching angle based on intuition informed by his experience with salt crystal growth. That is, for each generation the average branching angle θ will be prescribed by the author. To compute this angle, the standard deviation for R_x and R_y are calculated from the prescribed branch angle and the known average branch length for each generation, as explained below. The standard deviation required for an average angle formed by the branches with respect to the normal, illustrated in Figure 3.9, is obtained as follows.

In order to determine the standard deviation, the average or expected value of the Probability Density Function (PDF) for a half-normal distribution must be calculated. A half-normal distribution is used for the expected value because the same angle will result from a positive value of x and y as for a negative value of x and y, as illustrated in Figure 3.9. A half-

normal PDF is determined by multiplying the PDF of a normal distribution by two. The PDF, denoted by $f(x)$ for a normal distribution centered at zero, is

$$f(x) = \frac{1}{\sigma_x\sqrt{2\pi}} e^{-\frac{(x)^2}{2\sigma_x^2}} \ . \tag{4.1}$$

In Equation 4.1 σ_x is the standard deviation and x is the value of the random variable. The expected value is

$$E[x] = \int_0^\infty x f(x) dx \ . \tag{4.2}$$

The expected value of the half-normal distribution is determined by substituting Equation 4.1 into Equation 4.2 and multiplying by two, which yields

$$E[x] = \int_0^\infty \frac{2x}{\sigma_x\sqrt{2\pi}} e^{-\frac{(x)^2}{2\sigma_x^2}} dx \ . \tag{4.3}$$

The expected value of the half-normal distribution is then calculated,

$$\mu_x = E[x] = \frac{\sqrt{2}}{\sqrt{\pi}}\sigma_x \ . \tag{4.4}$$

The expected value represents the mean value for a random number with a half-normal distribution. The same process is used to find the expected value or mean value for a random number with respect to y. From this point on $\mu_{x,y}$ will denote the mean of a half-normal distribution for either x or y.

Figure 4.3 illustrates calculation of the standard deviation for the random numbers R_x and R_y and the mean for the random number R_z from the branching angle and the known average branch length.

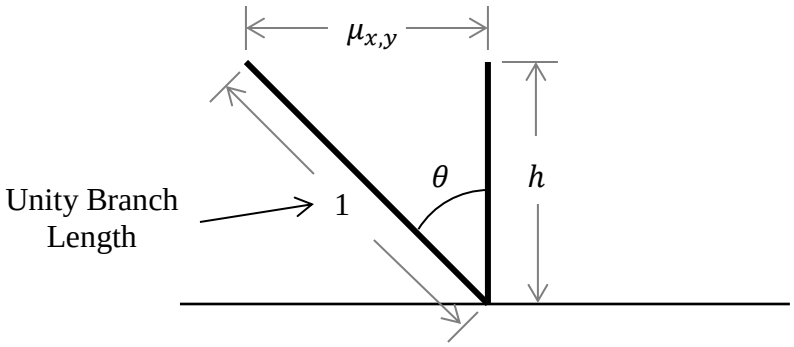

Figure 4.3: Average branching angle illustration.

The mean of x or y coordinates for a half-normal distribution and the known average branch length are related using the trigonometric identity

$$\sin\theta = \frac{opposite}{hypotenuse} \ , \tag{4.5}$$

where *opposite* is equal to the mean of a half-normal distribution in either x or y and the *hypotenuse* is equal to the unity branch length. Equation 4.5 may be rearranged to yield

$$\mu_{x,y} = \sin\theta \ . \tag{4.6}$$

Setting Equations 4.4 and 4.6 equal to each other and solving for the standard deviation in terms of θ yields

$$\sigma = \frac{\sqrt{\pi}\sin\theta}{\sqrt{2}} \ . \tag{4.7}$$

Equation 4.7 is the standard deviation required in order to create an average branching angle provided by the author.

Figure 4.4 (a) illustrates standard normal distributions with three different values of standard deviation. Figure 4.4 (b) illustrates the corresponding half-normal mean for x and y coordinates. It is important to note that the mean shown in Figure 4.4 (b) represents the half-normal mean of the PDF in Figure 4.4 (a).

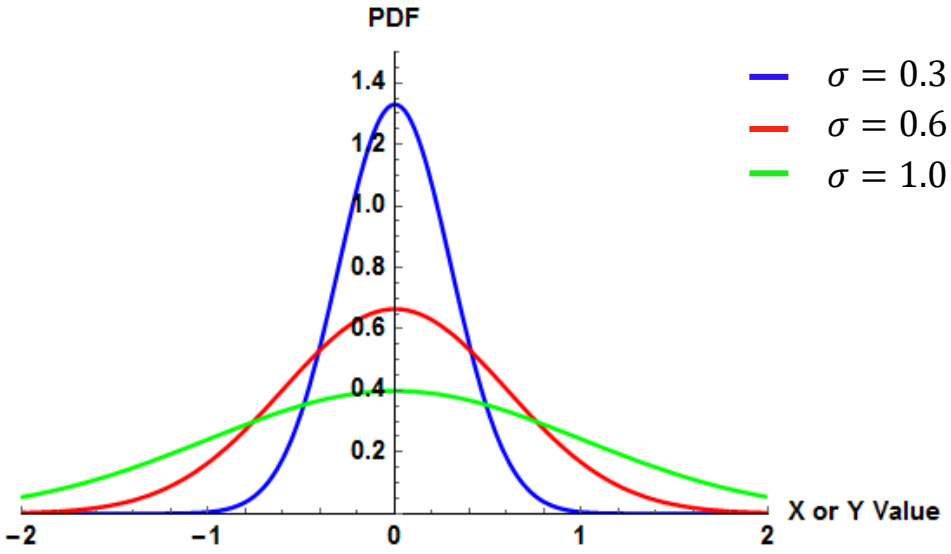

(a)

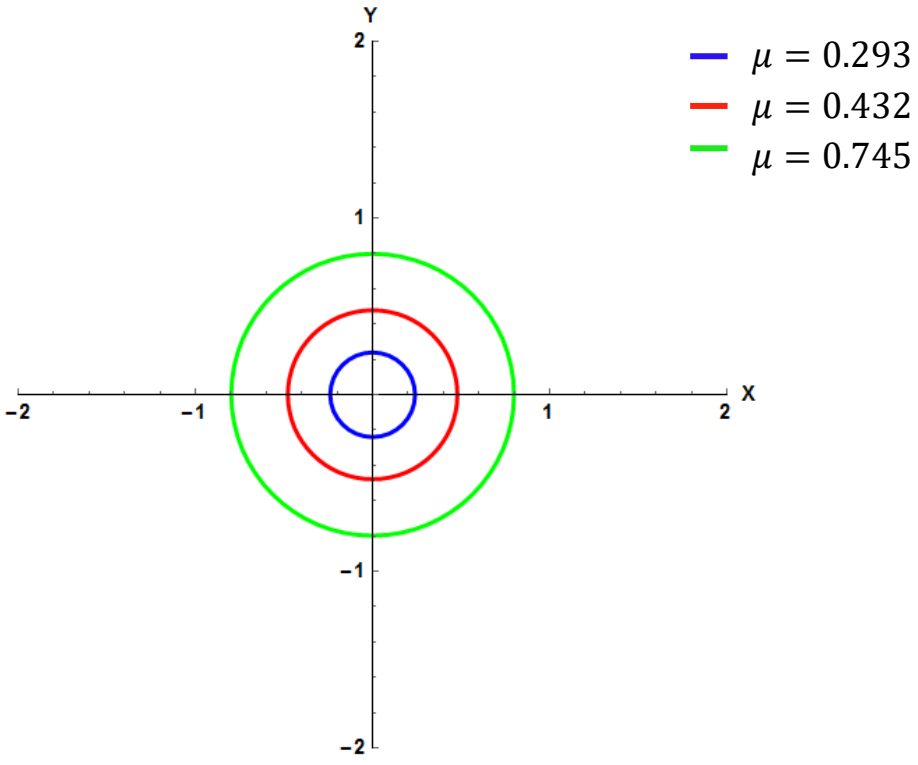

(b)

Figure 4.4: (a) Probability Density Function (PDF) corresponding to values of standard deviation shown, and (b) The corresponding mean values for x and y coordinates.

The average height is calculated by using the trigonometric identity

$$\cos\theta = \frac{adjacent}{hypotenuse} \ , \tag{4.8}$$

where the *adjacent* side is equal to the height of the average branch length and the *hypotenuse* is once again equal to the unity branch length. Equation 4.8 may be rearranged to obtain

$$h = \cos\theta \ . \tag{4.9}$$

The mean value for R_z is calculated as

$$\mu_z = hS\gamma^g \ , \tag{4.10}$$

where S is the starting branch length, γ is the decay rate constant, and g is the current generation level.

Unity is assumed for the average branch length, as shown in Figure 4.3. As a result, the average branch length for any generation can be set by multiplying the unity branch length with the starting branch length and then with the decay rate constant raised to the power of the current generation.

The governing expressions used to generate new x, y, and z coordinates for three-dimensional growth are

$$x_{New} = R_x S\gamma^g \ , \tag{4.11}$$

$$y_{New} = R_y S\gamma^g \ , \tag{4.12}$$

and

$$z_{New} = R_z \ , \tag{4.13}$$

where S is the initial branch length, γ is a constant that defines the generation decay rate, and g is the current generation. The quantity R_z is a normally distributed random number with a mean value μ_z equal to the average branch height for each generation and fixed value of standard deviation chosen by the author. The quantities R_x and R_y are two different normally distributed

random numbers with a true mean value of zero and a standard deviation σ whose value varies according to the branching angle θ.

Table 4.1 summarizes all of the parameters and relationships used to simulate gold-black growth.

Table 4.1: Integration of physical relationships into the gold-black deposition numerical simulation.

Computer Simulation Representation	Symbol	Integration description
Number of Nucleation Sites (per unit area)	N	• Nucleation sites are randomly distributed over a fixed range. They represent the first influence of evaporation rate.
Generation Limitation	G	• A limitation on the number of generations based on a minimum branch size limit. This represents the second influence of evaporation rate.
Average Branching Angle	θ	• Normally distributed random numbers with a variable standard deviation in terms of the branching angle. They represent pressure changes.
Decay Rate Constant	γ	• The decay rate constant is a number between zero and unity that decreases the branch size as the generation level is increased. This represents the first influence of temperature.
Starting Branch Length	S	• The starting branch length is the length at which the branches start. This represents the second influence of temperature.

In summary, (1) Gold-black deposition is simulated based on observations of salt crystal growth. (2) Parameters determined from the literature are used to adjust the computer simulation to visually match gold-black deposits in the literature.

4.3 Gold-Black Simulation Results

The resulting simulation produces gold-black deposits that are similar in appearance to images of salt crystals, as illustrated by Figure 4.5. The results illustrated in Figure 4.5 establish that a process similar to DLA, described in Section 2.5, can be used to simulate a gold-black deposit based on fractal geometry. The process described above is not exactly the same as DLA but rather is a guided process driven by random numbers from statistical distributions.

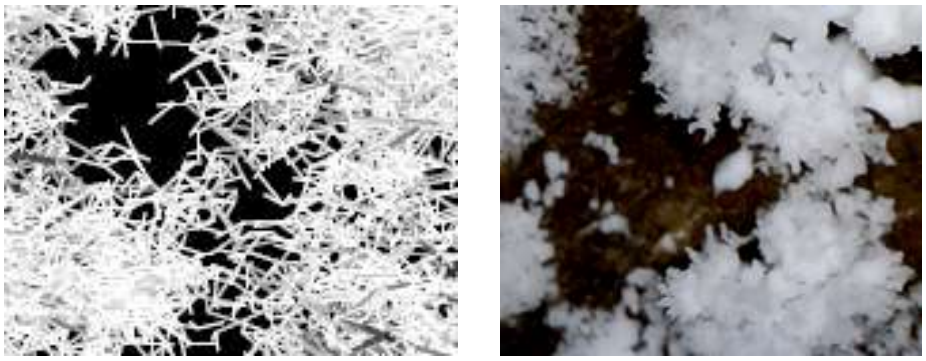

(a) (b)

Figure 4.5: Visual comparison between (a) computer simulation and (b) salt crystals grown by the author.

The resulting simulated structure representing all of the salt crystal observations presented in Section 3.3 is illustrated in Figure 4.6. Figure 4.6 shows nucleation sites, a coarse structure terminally and a fine structure initially, and branching achieved with prescribed angles. The gradual reduction in branch size due to the decay rate constant γ may be observed by visually following one of the outer branches to the top. The branching pattern is well represented by two or three branches from each node. Reconnection points are also visible in Figure 4.6 at crossing branches. The differences in generation levels are shown by a color gradient from black, as the first generation, to white, as the final generation.

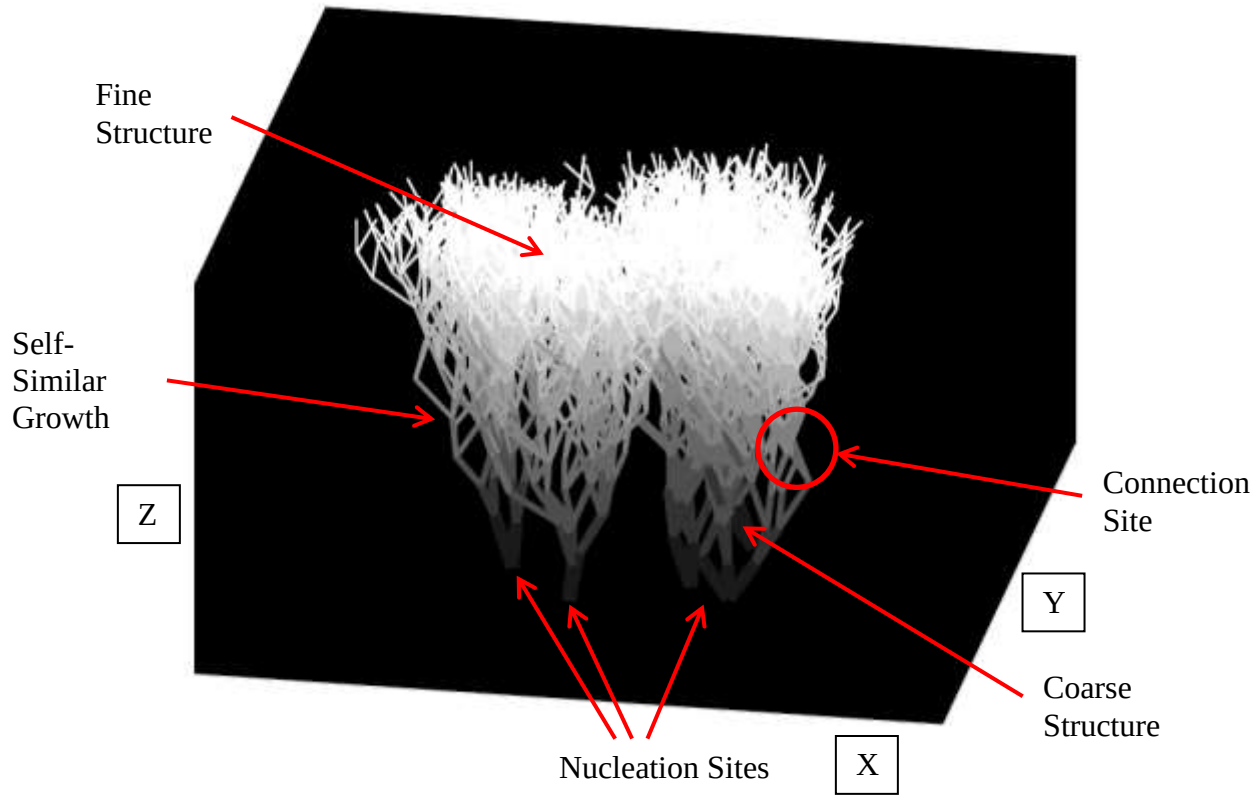

Figure 4.6: Simulation with various features indicated.

4.4 Comparison Between Gold-Black Simulation and Actual Gold-Black Deposits

The simulated gold-black growth compares well to images of gold-black deposits from the literature. Specifically, two simulated gold-black deposits created using different sets of parameters are compared with actual deposits reported by two different sources.

Figure 4.7 is a direct comparison of a gold-black deposit from Ilisa, *et al.* [2010] with a computer simulation of gold-black.

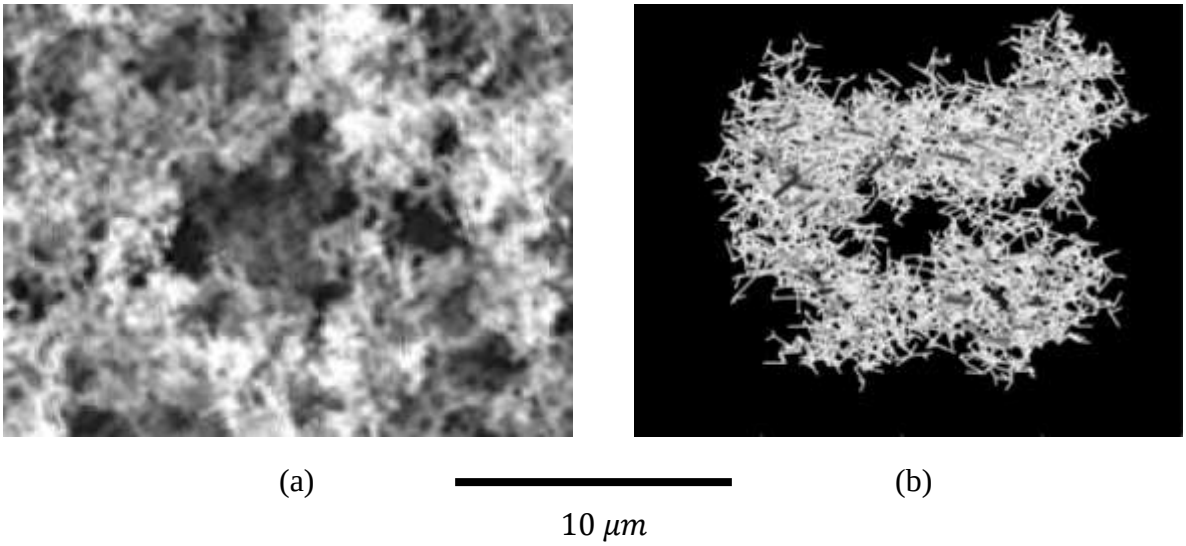

Figure 4.7: Direct comparison between plan views of (a) a gold-black deposit [Ilias, S., P. Topart, C. Larouche, P. Beaupré, D. Gay, C. Proulx, T. Pope, C. Alain "Deposition and Characterization of gold-black coatings for thermal infrared detectors" *SPIE*, Vol. 7750, 2010.] Used under fair use, 2015, and (b) the corresponding gold-black simulation.

The images in Figure 4.7 compare well visually. The image from Ilisa, *et al.* [2010] were taken with an electron microscope and shows late-generation growth in white, mid-growth in gray, and black areas where presumably no growth has occurred. The simulation reproduces these same characteristics. Near and far areas are difficult to distinguish in plan view of the simulation, in which lighter colors represent final growth and darker colors represent initial growth. The branch sizes seem to compare well when viewed closely. The overall height of the gold-black deposit is comparable to the overall height of the simulated deposit which is approximately 30 μm. The 10-μm scale applies to both images.

Figure 4.8 is a direct comparison of a gold-black deposit from Panjwani, *et al.* [2014] and the corresponding computer simulation of gold-black.

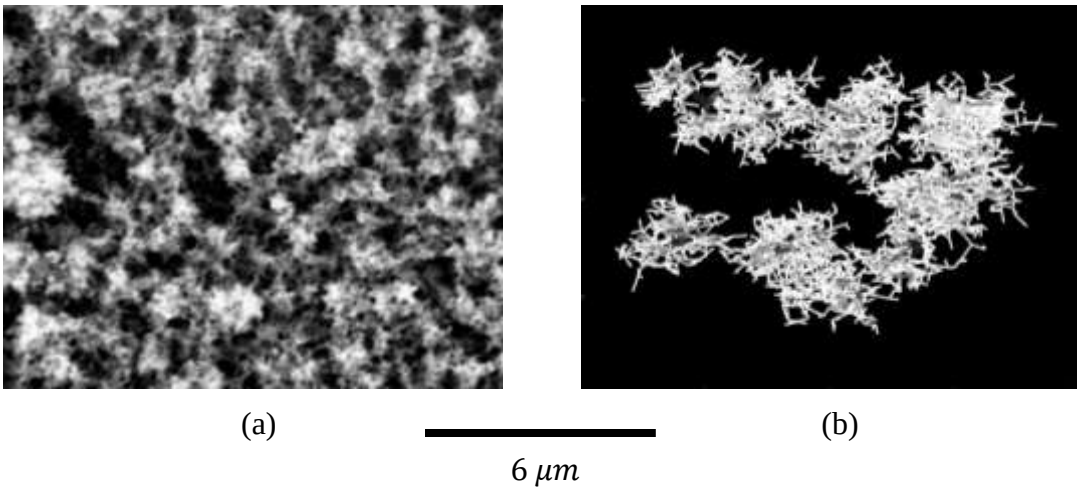

Figure 4.8: Direct comparison between plan views of (a) a gold-black deposit [Panjwani, Deep., Mehmet Yesiltas, Simranjit Singh, Enrique Del Barco, R. E. Peale, Carol Hirschmugl, Julia Sedlemair, "Stencil Lithography of gold-black IR absorption coatings" *Infrared Physics & Technology*, Vol. 66, pp. 1-5, 2014.] Used under fair use, 2015, and (b) a simulated gold-black deposit.

The images in Figure 4.8 also compare rather well. The computer simulation has larger clusters of gold-black growth as compared to the actual gold-black deposit. The gold-black deposits shown in Figure 4.8 correspond to a much lower pressure than the gold-black deposits shown in Figure 4.7. To match the computer simulation to the actual deposit in Figure 4.8, the branching angle was decreased by the author to produce more sparsely spaced gold-black growth.

To summarize, a computer program has been created with an adjustable set of parameters, listed in Table 4.1, which can in principle be used to match any gold-black deposit found in the literature. Figures 4.7 and 4.8 demonstrate the effectiveness and versatility of the gold-black computer simulation in matching actual gold-black deposits reported in the literature. At this point the simulated geometry of gold-black can be directly related to electrical circuits, as indicated in Section 2.6.

Chapter 5: Gold-Black Structure as Independent Electrical Circuits

5.1 Relationship of Electrical Circuits to Gold-Black Simulation

In order to develop a theoretical model for the absorption of thermal radiation by the simulated gold-black fractal geometry created in Chapter 4, an appropriate analogy must be drawn between the simulated physical structure and its interaction with thermal radiation. This analogy takes the form of a collection of electrically independent series circuits, each consisting of an inductor (L), a capacitor (C), and a resistor (R). The introduction of RLC circuits is encouraged by ideas from the literature introduced in Section 2.6 and by discussions between the author and his thesis advisor. An electrical circuit was chosen as a basis for a theoretical model because thermal radiation is an oscillating electro-magnetic field that propagates through space and which is capable of inducing an alternating current in an electrical circuit. Figure 5.1 shows one polarization of an EM wave propagating downward. Naturally polarized radiation consists of two such polarizations whose electric field vectors are mutually orthogonal. For clarity, only one of the two polarizations is shown here. In the figure $\vec{E}$ is the electric field strength vector, $\vec{H}$ is the magnetic field strength vector, and $\vec{P}$ is the Poynting vector representing the power flux carried by one polarization. The electro-magnetic field associated with thermal radiation is posited to interact with the gold-black fractal geometry much like a radio wave interacts with an antenna.

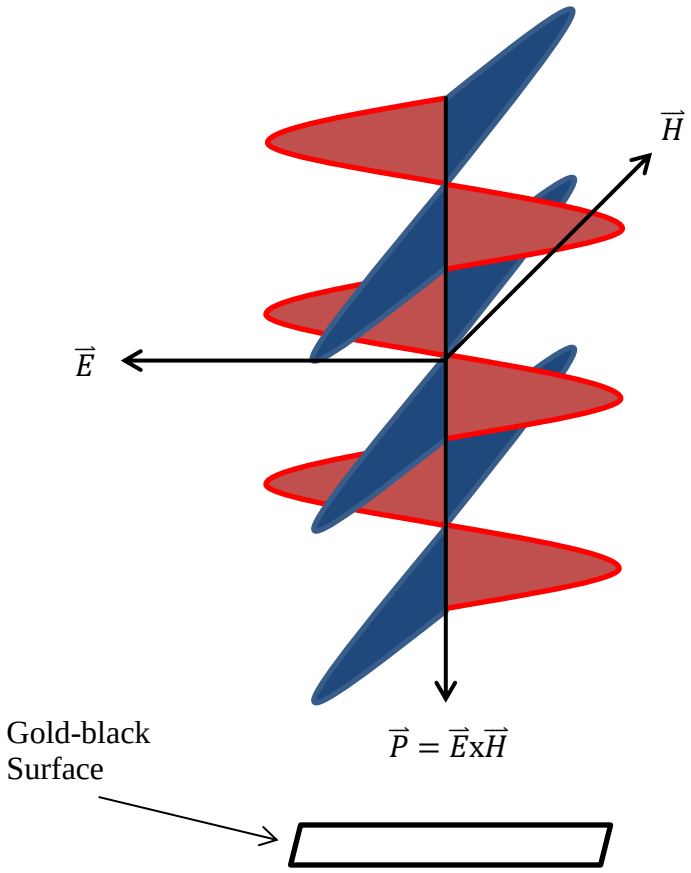

Figure 5.1: One polarization of an electro-magnetic wave propagating downward.

The simulated gold-black growth is thought to organize itself into independent electrical circuits as suggested by the highlighted regions in Figure 5.2, which shows loops formed by interconnecting branches of various dimensions. The connections described in Section 4.2 allow for branch loops of various sizes to be formed within each generation. Such loops can be completed either physically or, far more likely, by means of capacitive coupling. The absorption of thermal radiation is due to the interaction between an electro-magnetic wave and the branch loops formed during gold-black growth. The electrical component of the electro-magnetic wave induces current flow around a branch loop, as indicated in Figure 5.3. For efficient coupling to occur, the size of the branch loop needs to be on the order of the wavelength of the incident electro-magnetic radiation. As the wavelength of the incident electro-magnetic radiation

increases, the size of the branch loops in which the current is induced increases accordingly. Thus, the branch loops outlined in violet in Figure 5.2 have a characteristic dimension of approximately 0.5 µm, the branch loops outlined in red have a characteristic dimension of approximately 1 µm, and the branch loops outlined in blue have a characteristic dimension of approximately 2 µm.

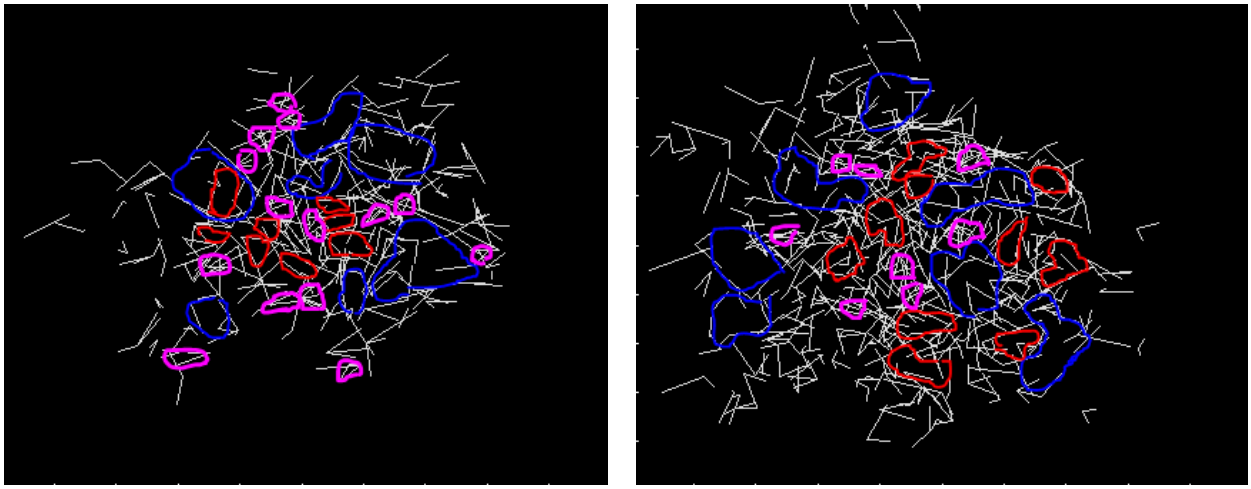

(a) (b)

Figure 5.2: A single generation of simulated gold-black with branch loops highlighted; (a), generation level is equal to six. (b), generation level is equal to seven.

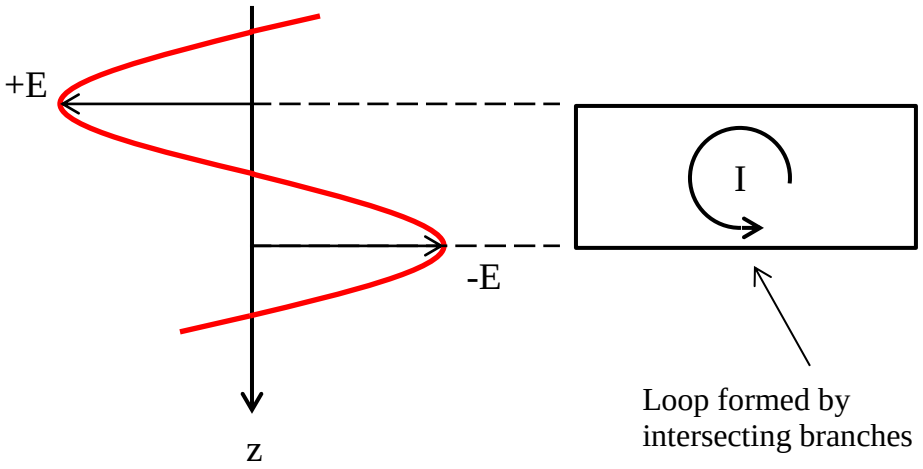

Figure 5.3: Oscillating current in a loop of gold-black branches induced by the electric component of an incident electro-magnetic wave.

5.2 Definition of RLC Circuits

Circuits are created by replacing each branch loop shown in Figure 5.2 with a series arrangement of resistors, inductors, and capacitors. The components are envisioned to be arranged as shown in Figure 5.4.

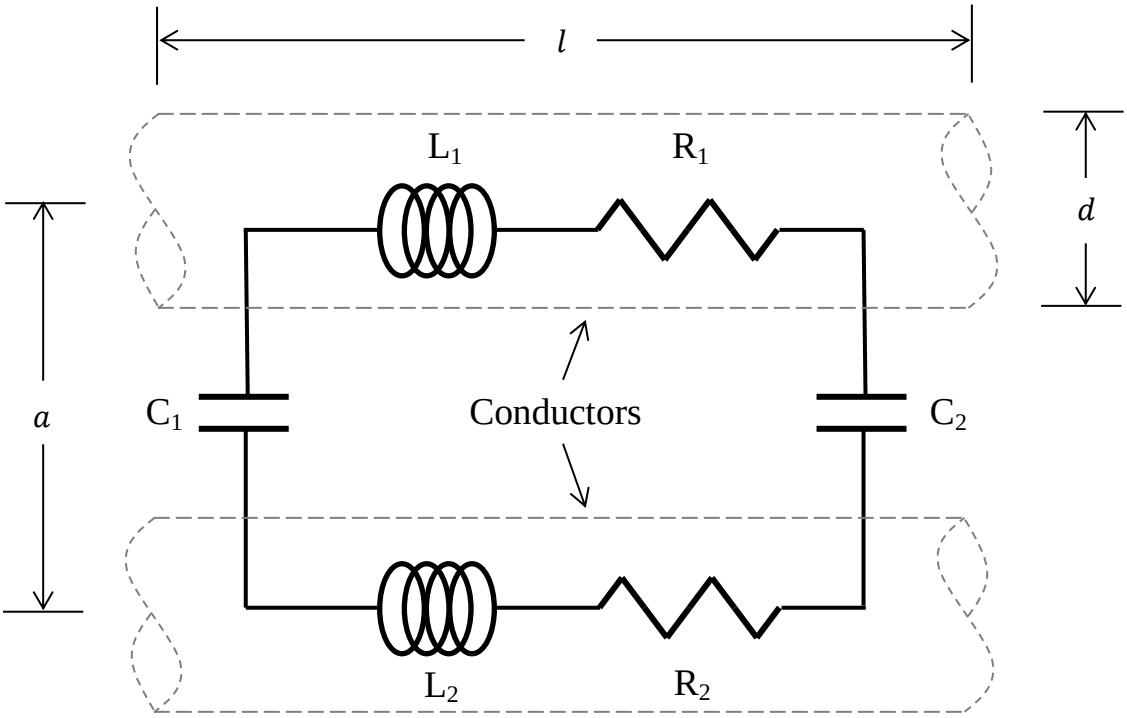

Figure 5.4: Circuit representation of a single branch loop.

The capacitances, identified as C_1 and C_2 in Figure 5.4, are determined by assuming each branch loop is composed of two parallel conductors. The capacitance between two parallel conductors is given by Jackson [1975],

$$C = \left(\frac{1}{C_1} + \frac{1}{C_2}\right)^{-1} = \frac{\pi\epsilon_0 l}{\ln\left(\frac{a}{d} + \sqrt{\frac{a^2}{d^2} - 1}\right)}, \tag{5.1}$$

where d is the diameter of one conductor, a is the distance between two parallel conductors, ϵ_0 is the permittivity of free space, and l is the length of one conductor. The diameter d is

arbitrarily assumed to be one tenth of the characteristic dimension of the branch loop, a is arbitrarily assumed to be twice the diameter of a single branch at a particular generation, and l corresponds to the characteristic dimension of the branch loop. The characteristic dimension of a particular branch loop is assumed to be on the order of the wavelength of incident thermal radiation.

The inductances, identified as L_1 and L_2 in Figure 5.4, are determined by again assuming each branch loop to be composed of two parallel conductors. The inductance associated with two parallel conductors is given by Rosa [1908],

$$L = L_1 + L_2 = \frac{\mu_0 l}{\pi} \ln\left(\frac{a}{d} + \sqrt{\frac{a^2}{d^2} - 1}\right), \tag{5.2}$$

where d is the diameter of one conductor, a is the distance between two parallel conductors, μ_0 is the permeability of free space, and l is the length of one conductor. Once again, in using Equation 5.2 the diameter d is arbitrarily assumed to be one tenth of the characteristic dimension of the branch loop, a is arbitrarily assumed to be twice the diameter of a single branch at a particular generation, and l corresponds to the characteristic dimension of the branch loop. As before, the characteristic dimension of a particular branch loop is assumed to be on the order of the wavelength of the incident thermal radiation.

The resistances, identified as R_1 and R_2 in Figure 5.4, are determined by assuming each branch loop to be two parallel conductors connected to each other at the ends, either physically or through capacitive coupling. The resistance of a gold conductor of length l and cross-sectional area A_c is given by,

$$R = R_1 + R_2 = \frac{r_{gold} l}{A_c} \tag{5.3}$$

The resistivity r_{gold} is defined by Equation 5.3. In this work the resistivity for bulk gold at 300 K is used, and A_c is the cross-sectional area of one branch. The length of the electrical conductor corresponds to the characteristic dimension of a particular branch loop, which is once again assumed to be on the order of the wavelength of the incident thermal radiation.

Once the values for the components in Figure 5.4 have been determined, they are combined in series to produce the RLC circuit shown in Figure 5.5.

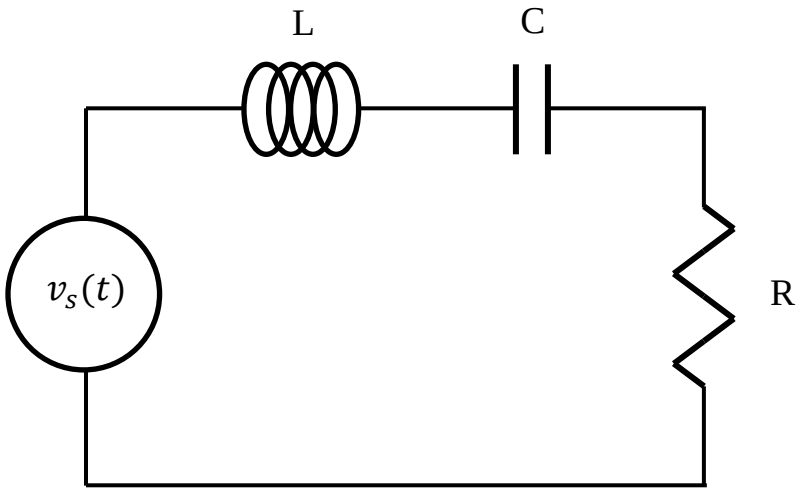

Figure 5.5: Series RLC circuit.

The equivalent capacitance, denoted by C in Figure 5.5, is calculated by

$$C = \left(\frac{1}{C_1} + \frac{1}{C_2}\right)^{-1} , \tag{5.4}$$

the equivalent inductance, denoted by L in Figure 5.5, is calculated by

$$L = L_1 + L_2 , \tag{5.5}$$

and the equivalent resistance, denoted by R in Figure 5.5, is calculated by

$$R = R_1 + R_2 . \tag{5.6}$$

The RLC circuit in Figure 5.5 is the basis of a theoretical model for the absorption of thermal radiation by gold-black. A series RLC circuit is used to represent each branch loop. The

structure of the circuit is suggested by the fact that each branch loop will exhibit an equivalent resistance, inductance, and capacitance. The fact that the circuit is tunable means that its impedance is a minimum, equal to the resistance, at its resonate frequency. Since a gold-black deposit is created with many generations, the result will be similar to the ultra-wideband fractal antennas already discussed in Section 2.5.

The voltage source, denoted $v_s(t)$ in Figure 5.5, is related to the electric field component of the incident EM radiation as illustrated in Figure 5.3 and may be written

$$v_s(t) = ve^{j(\omega t)} \ . \tag{5.7}$$

In Equation 5.7, v is the amplitude, ω is the angular frequency, and t is time. The angular frequency relates the alternating voltage source to the incident monochromatic radiation according to

$$\omega = \frac{2\pi c_0}{\lambda} \ . \tag{5.8}$$

In Equation 5.8, c_0 is the speed of light in a vacuum and λ is the wavelength of the incident electro-magnetic radiation.

5.3 Simplifying Assumptions

Various simplifying assumptions are used to reduce the complexity of the problem at hand.

- The RLC circuits created for each branch loop are assumed to be electrically independent from each other.
- Radiation incident at different wavelengths does not interfere; i.e., the principle of frequency multiplexing applies.
- Radiation is treated as steady-state.

- The incident EM field diminishes in magnitude for RLC circuits deeper in the gold-black deposit due to absorption.
- All components in Figures 5.4 and 5.5 are assumed discrete.
- Incident electro-magnetic waves are assumed to be naturally polarized and monochromatic.
- The characteristic dimension of a branch loop is considered to be one-half wavelength because half-wave antennas have the highest efficiency.

5.4 RLC Circuit Analysis

Upon application of the simplifying assumptions, RLC circuit behavior is applied for each branch loop with appropriate values for resistance, inductance, and capacitance.

The model of absorption of thermal radiation within a gold-black growth such as those simulated in Chapter 4 is based on

$$\mathrm{L}\frac{d^2q}{dt^2} + \mathrm{R}\frac{dq}{dt} + \frac{q}{\mathrm{C}} = ve^{j(\omega t)} \ , \tag{5.9}$$

where q is the electric charge. The model represented by Equation 5.9 is an inhomogeneous second-order ordinary differential equation with a sinusoidal source term. Sought is the steady-state voltage across the resistor as a function of frequency, which can be interpreted as power absorption in the loop at a given wavelength. The electrical charge is assumed to have the form

$$q = q_0 e^{j(\omega t+\phi)} \ , \tag{5.10}$$

where q_0 is the amplitude of the electric charge and ϕ is the relative phase angle. The first two derivatives of the electric charge are

$$\frac{dq}{dt} = q_0(j\omega)e^{j(\omega t+\phi)} \tag{5.11}$$

and

$$\frac{d^2q}{dt^2} = q_0(j\omega)^2 e^{j(\omega t+\phi)} \ . \tag{5.12}$$

Equations 5.10 through 5.12 are substituted into Equation 5.9 and simplified to yield

$$\mathrm{L}q_0(j\omega)^2 + \mathrm{R}q_0(j\omega) + \frac{q_0}{\mathrm{C}} = ve^{-j\phi} \ . \tag{5.13}$$

The angular frequency ω in radians per second is related to frequency f in Hertz by

$$\omega = 2\pi f \ . \tag{5.14}$$

When Equation 5.14 is substituted into Equation 5.13, there results

$$\mathrm{L}q_0(j2\pi f)^2 + \mathrm{R}q_0(j2\pi f) + \frac{q_0}{\mathrm{C}} = ve^{-j\phi} \ . \tag{5.15}$$

The current may be expressed in terms of electric charge and frequency as

$$I = q_0 2\pi f \ . \tag{5.16}$$

Rearranging Equation 5.15 and introducing Equation 5.16 yields

$$I\left[-\mathrm{L}(2\pi f) + \mathrm{R}j + \frac{1}{2\pi \mathrm{C}f}\right] = ve^{-j\phi} \ . \tag{5.17}$$

Finally Equation 5.17 is simplified by dividing the entire equation by current and multiplying by $-j$ to yield

$$j2\pi f\mathrm{L} + \mathrm{R} - \frac{j}{2\pi f\mathrm{C}} = -j\frac{ve^{-j\phi}}{I} \ . \tag{5.18}$$

The left-hand side of Equation 5.18 is the impedance Z in terms of the components of the RLC circuit; i.e.,

$$j2\pi f\mathrm{L} + \mathrm{R} - \frac{j}{2\pi f\mathrm{C}} = Z \ . \tag{5.19}$$

Ohm's law is used to compute the current I through the circuit,

$$I = \frac{v}{Z} \ . \tag{5.20}$$

The voltage across the resistor,

$$v_R = I\mathrm{R}\ , \tag{5.21}$$

is given by Ohm's law since the current is the same for each component of a series circuit. Equations 5.19 and 5.20 may now be substituted into Equation 5.21 to yield

$$\frac{v_R}{v} = \frac{1}{1 + j\left(\frac{2\pi f\mathrm{L}}{\mathrm{R}} - \frac{1}{2\pi f\mathrm{CR}}\right)}\ . \tag{5.22}$$

The magnitude of Equation 5.22 describes the real part of the voltage across the resistor. The real part of the dimensionless voltage across the resistor at a given frequency is

$$\frac{V_R}{V} = \frac{1}{\sqrt{1 + \left(\frac{2\pi fL}{R} - \frac{1}{2\pi fCR}\right)^2}}\ . \tag{5.23}$$

In Equation 5.23, V_R and V are respectively the magnitude of the voltage across the resistor and the input voltage. The frequency at which the voltage across the resistor in the RLC circuit is a maximum is the resonant frequency. The resonant frequency occurs when the reactance of the inductor and the capacitor are equal but opposite in sign. The resonant frequency f_{res} in terms of inductance and capacitance may be expressed by

$$f_{res} = \frac{1}{2\pi\sqrt{LC}}\ . \tag{5.24}$$

Figure 5.6 shows the voltage across the resistor as a function of frequency for one branch loop at several generation levels for incident radiation at a wavelength of 1 μm or a frequency of 3.0×10^{15} Hz.

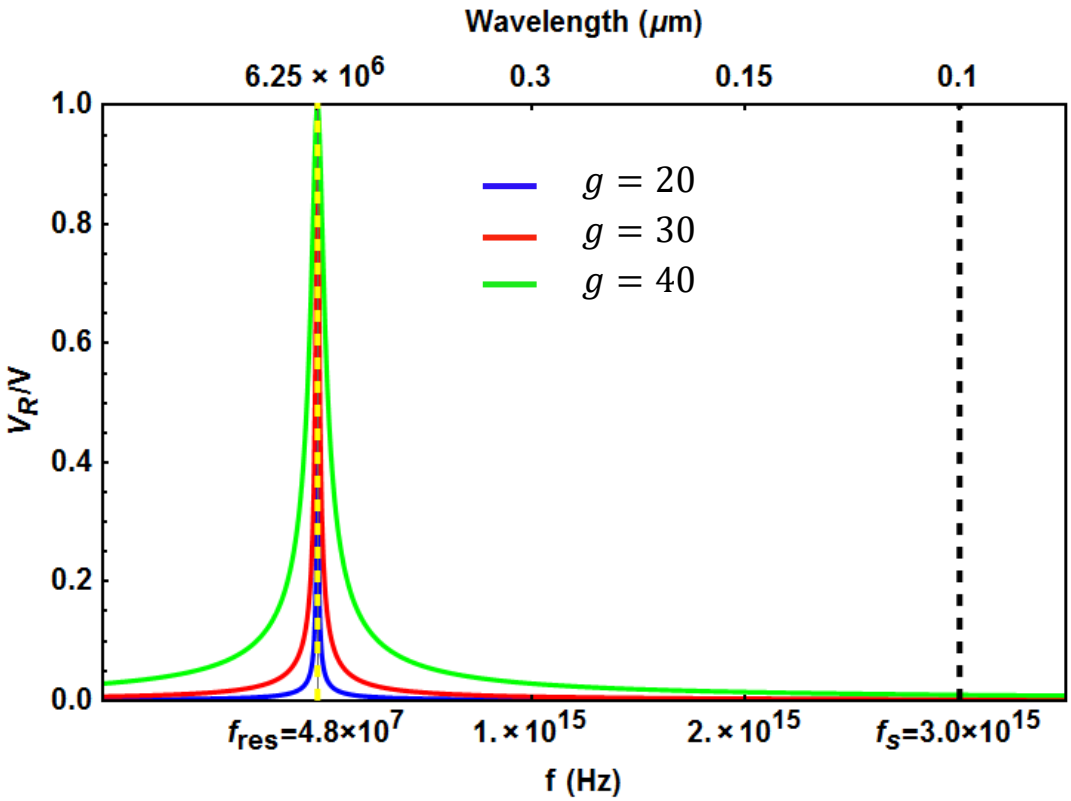

Figure 5.6: Voltage across the resistor as a function of frequency for 20, 30, and 40 generations.

The voltage across the resistor is extremely small. However, each generation consists of many branch loops. This means that the power conversion associated with each of these loops sums to a much greater value. Figure 5.6 suggests that the inductive component of the overall impedance, $|X_L| = \omega L$, dominates at frequencies representative of visible and near infrared radiation. That is, most of the source voltage is developed across the inductor at the expense of the resistor. The capacitor is essentially a short circuit at these frequencies, and the overall circuit is then essentially a low-pass filter.

5.5 Determination of Absorption as a Function of Wavelength

The absorption of thermal radiation by gold-black is equal to the power absorbed by the resistor shown in Figure 5.5. It is convenient to represent absorption values in terms of wavelength; therefore frequency is converted to wavelength,

$$\lambda = \frac{c_0}{f} \ . \tag{5.25}$$

The input voltage is normalized to unity in order to represent voltages across the resistor from zero to unity. Thus, setting the input voltage V to unity in Equation 5.23, V_R now represents the voltage across the resistor for each branch loop. Once the voltage across the resistor is known, the power absorbed by the resistor is given by

$$P_{R,\lambda,g} = \frac{V_R^2}{\mathrm{R}} \ . \tag{5.26}$$

In Equation 5.26, $P_{R,\lambda,g}$ is the power absorbed by the resistor for a given wavelength λ and generation level g under consideration, assuming the input voltage $V = 1$.

Once the power absorbed by one branch loop for a given frequency and generation level is determined, the power absorbed by an entire simulated geometry can be calculated by multiplying the power absorbed for one branch loop by the total number of branch loops for a given generation,

$$P_{abs,\lambda,g} = \left[\frac{P_{R,\lambda,g}}{P_{0,\lambda}} B_g \left(M_{\lambda,g}\right)^{\pm 1}\right] \left(P_{0,\lambda} - P_{abs,\lambda,g+1}\right) \ . \tag{5.27}$$

In Equation 5.27, $P_{abs,\lambda,g}$ is the power absorbed by all of the branch loops for a given generation and a given wavelength, $P_{0,\lambda}$ is the incident power at wavelength λ, $M_{\lambda,g}$ is a multiplier, and B_g is the number of branch loops for a given generation. The term $\frac{P_{R,\lambda,g}}{P_{0,\lambda}}$ is the fraction of the

incident monochromatic power absorbed in generation g. The fraction of power absorbed for each generation is multiplied by the fraction of power having passed through the outer layers of generations. By multiplying the number of branches B by the multiplier M, the simulated gold-black geometry developed in Chapter 4 is directly related to the theoretical model developed here.

The multiplier represents the fraction of branch loops present in any given generation for a particular wavelength of incident thermal radiation. The multiplier is expressed in terms of wavelength and the physical branch length of each generation; i.e.,

$$M_{\lambda,g} = \frac{\lambda}{l_{br,g}} \ . \tag{5.28}$$

In Equation 5.28 $l_{br,g}$ is the average length of a branch for a given generation and λ is the wavelength of incident thermal radiation. The multiplier is always a number between zero and unity. It ensures that the maximum number of branches occurs when the average branch length is on the order of the incident thermal radiation. Figure 5.7 illustrates the multiplier as a function of wavelength for a given average branch length at a given generation.

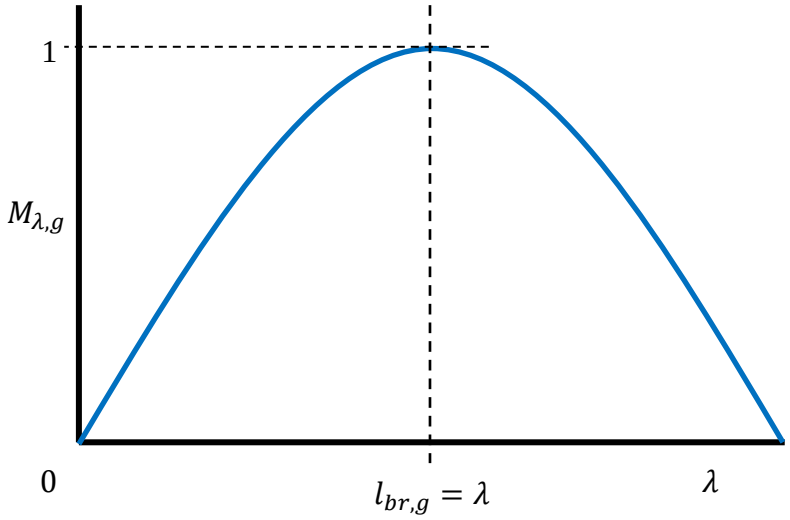

Figure 5.7: Illustration of the multiplier as a function of wavelength.

For example, if the wavelength is short compared to the average branch length, the multiplier will reduce the number of available branch loops. However, this is also true when the wavelength is large compared to the average branch length, in which case the multiplier is raised to the -1 power. Figure 5.8 is the antenna factor (AF) of a dipole antenna as a function of the polar angle (Θ).

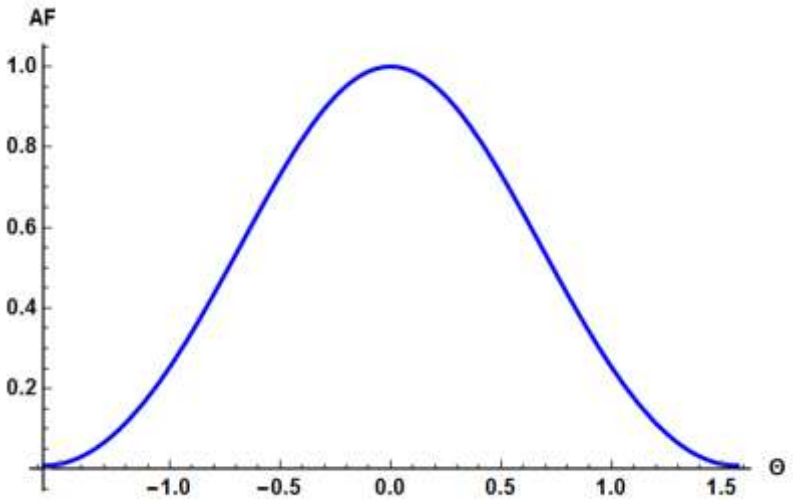

Figure 5.8: Antenna factor (AF) of a dipole antenna as a function of the polar angle (Θ).

Figures 5.7 and 5.8 are very similar. The visual comparison between the two suggests that there is a relationship between the multiplier and the antenna factor of a dipole antenna.

The quantity B in Equation 5.27 represents the total number of branches for a gold-black simulation in a given generation. Ideally the total number of branches for each generation would be obtained by the gold-black simulation developed in Chapter 4. However, computational limits were encountered when gold-black simulations were attempted with more than ten generations. An extrapolation curve was needed in order to extend results to generation levels beyond ten. Ten generations were created for each gold-black simulation and a third-order

extrapolation curve was then fitted to obtain results for additional generations. A third-order polynomial was used because good agreement was observed in the range of the available results. The extrapolation curve used throughout this chapter is illustrated in Figure 5.9 where the curve represents the extrapolation and the corresponding results are represented as solid dots.

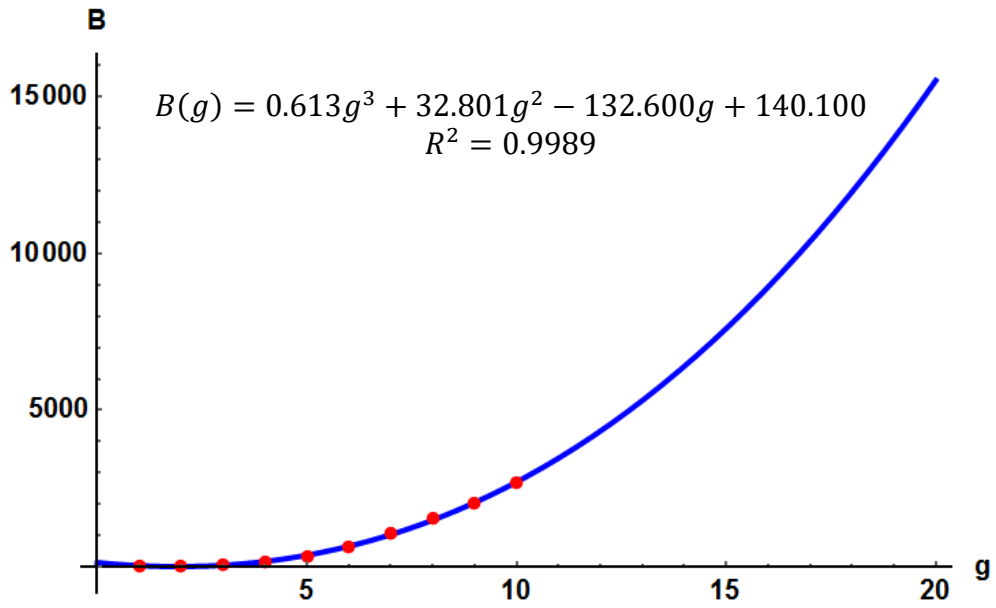

Figure 5.9: Third-order polynomial based on results for ten generations (equation and R^2 value shown) used to extrapolate to larger numbers of generations.

The extrapolation curve obtained using the method of least squares shown in Figure 5.9 is

$$B(g) = 0.613g^3 + 32.801g^2 - 132.600g + 140.100 \ . \tag{5.29}$$

The corresponding R^2 value associated with Equation 5.29 is in excess of 0.9989. An extrapolation curve is a useful tool; however, it is well known that results obtained using it may be over or under estimated. The results may incur significant error since the extrapolation curve has a strong influence on the link between the simulated geometry and the electrical circuit analysis.

Once the multiplier and number of branches have been established for each generation, the power absorbed by the resistor can be summed for a particular wavelength and over all generations as

$$\alpha_\lambda = \frac{P_{total,\lambda}}{P_{0,\lambda}} = \frac{1}{P_{0,\lambda}} \sum_{g=1}^{G} P_{abs,\lambda,g} \ . \tag{5.30}$$

In Equation 5.30 α_λ represents the monochromatic absorptivity of gold-black, $P_{total,\lambda}$ is the total power absorbed by all of the resistors for a gold-black simulation, $P_{0,\lambda}$ is the incident power at wavelength λ, and G represents the total number of generations.

The total dimensionless power absorbed for a given wavelength is assumed to be the spectral absorption, denoted by α_λ in Equation 5.30. The spectral absorptivity obtained using this model is plotted in Figure 5.9 as a function of wavelength. The Mathematica program used to create Figure 5.10 is available in Appendix B.

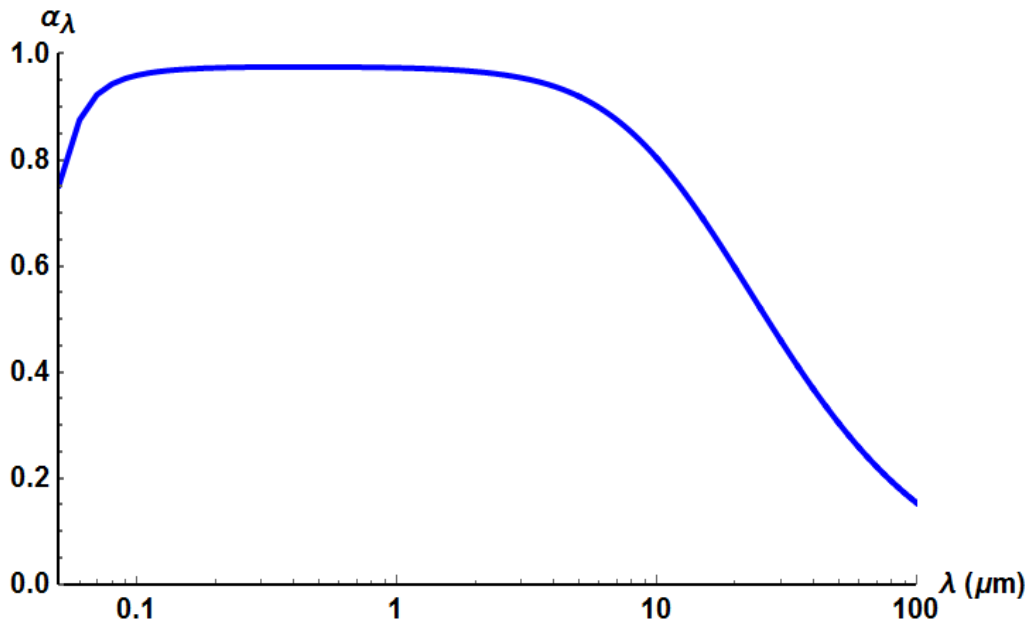

Figure 5.10: Absorption as a function of wavelength according to the theory developed in this thesis.

The spectral absorptivity shown in Figure 5.10 is excellent from 0.2 to 3 μm with values in excess of 0.95. Radiation at very short wavelengths and at very long wavelengths relative to the characteristic size of the loops is reflected due to inefficient coupling with the loops.

The process used to define a model for absorption of thermal radiation by gold-black may be summarized as follows:

- Branch loops are identified within the gold-black geometry as shown in Figure 5.2.
- The branch loops are replaced with equivalent series RLC circuits.
- Values for R, L, and C are computed based on the physical dimensions of the branch loops and branches.
- One RLC circuit is analyzed for each generation, with characteristic dimensions corresponding to the wavelength of the incident thermal radiation, to determine the power absorbed by the resistor.
- The number of branch loops for each generation is determined from the extrapolation function shown in Figure 5.9.
- The power absorbed by the resistor for one RLC circuit is multiplied by the number of branches for a particular generation and by a further multiplier.
- Absorption distributed over all generations is summed to obtain overall absorptivity values.

A theoretical model has been created for the monochromatic absorption of thermal radiation by gold-black. The model relates absorption values to the power absorbed by resistors in a large ensemble of series RLC circuits.

The absorption of thermal radiation in a gold-black deposit should be thought of as the result of two separate and distinct processes: (1) the conversion of electromagnetic energy into

thermal energy and (2) the subsequent transport of thermal energy through the structure to an underlying substrate where it is measured.

(1) Monochromatic electro-magnetic energy at a given wavelength permeates any gold-black deposit to which it is incident. Suitable combinations of individual branches making up the gold-black structure act both as antennas and distributed LRC circuits. The local electric field induces an oscillating electric current in these branches. The flow of this current through the electrical resistance of the branches converts a portion of the incident electro-magnetic energy into thermal energy by a process called Joulean (or Ohmic) heating. Thermal energy as the term is used here is commonly called "heat" but should more properly be called internal energy, $u = u(T)$.

(2) The role of gold-black as an absorber is to convert electromagnetic energy into thermal energy and then to deliver this thermal energy to an underlying substrate where it can be measured. This latter process, commonly called "heat transfer", is due solely to local temperature gradients. Heat transfer in this case is probably dominated by diffusion, although thermal radiation might also play a role.

The model developed in this thesis only deals with the first process. However, the second process is also crucial to the complete understanding of absorption of electro-magnetic radiation by gold-black.

Chapter 6: Theoretical Model Compared to Experimental Data

6.1 Comparison and Discussion of Results

Experimental monochromatic absorptivity results from the literature, reported in Section 2.3, are compared with the theoretical absorptivity results obtained in Chapter 5. Results from the theoretical model and the experimental data are shown to follow the same general trends. Also, absorptivity data at extremes of wavelength are examined to gauge if the theoretical model represents trends seen in the experimental data.

An iterative process, outlined in Section 1.4, has been used to obtain monochromatic absorptivity values. The first simulation run yielded unacceptably low absorptivity for the entire range of wavelengths examined. The average branch angle θ was subsequently increased as well as the generation limit G. The average branch angle was increased to encourage more branch loops per generation and the generation limit was increased to provide more branches. The corresponding parameter values required to produce a gold-black deposit with the absorption characteristics shown in Figures 5.7 are given in Table 6.1

Table 6.1: Parameters associated with absorptivity values given in Figure 5.7.

Name	Symbol	Value	Units
Number of Nucleation Sites (per unit area)	N	8	-
Generation Limitation	G	46	-
Branching Angle	θ	10	deg
Decay Rate Constant	γ	0.90	-
Starting Branch Length	S	3.3	μm

The monochromatic reflectivity is related to the absorptivity by

$$\rho_\lambda = 1 - \alpha_\lambda \ . \tag{6.1}$$

where ρ_λ is the monochromatic reflectivity. Equation 6.1 assumes that all incident thermal radiation is either absorbed or reflected.

Figures 6.1 and 6.2 show the theoretical results from Chapter 5 and experimental data from Section 2.3, respectively.

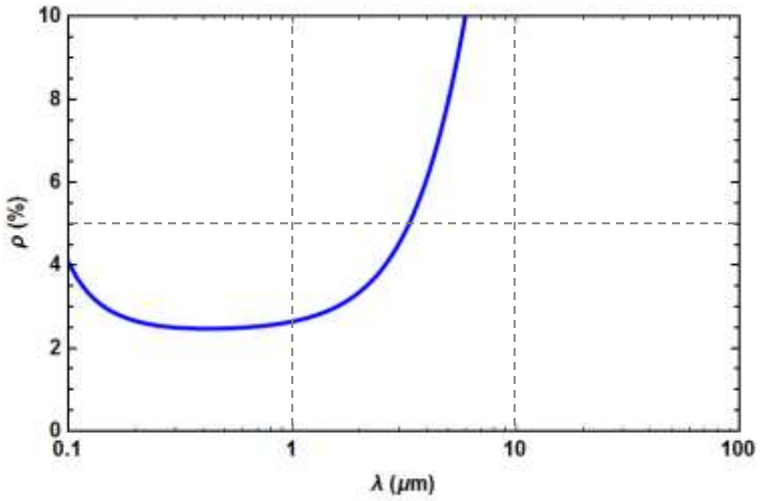

Figure 6.1: Theoretical variation of monochromatic reflectivity with wavelength according to the present theory.

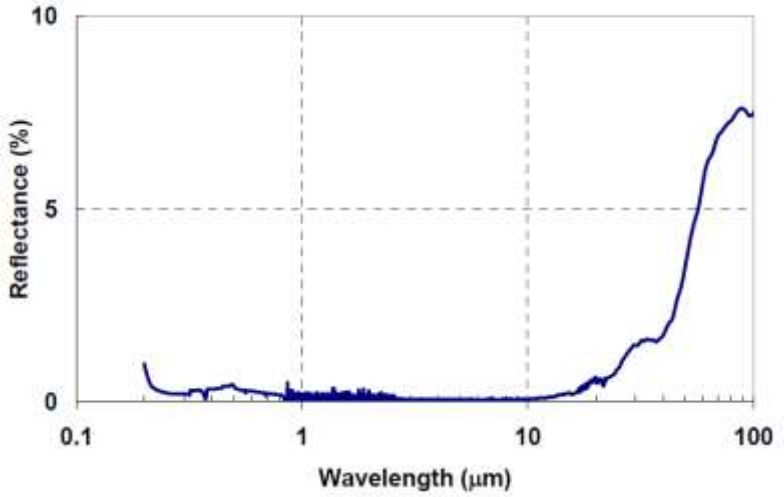

Figure 6.2: Experimental variation of monochromatic reflectivity with wavelength [Ilias, S., P. Topart, C. Larouche, P. Beaupré, D. Gay, C. Proulx, T. Pope, C. Alain "Deposition and Characterization of gold-black coatings for thermal infrared detectors" *SPIE*, Vol. 7750, 2010.] Used under fair use, 2015.

The theoretical results compare reasonably well with published data over part of the wavelength range examined; i.e. between 0.1 and 3 μm. However, the theoretical results show excessive reflectance values for wavelengths greater than 3 μm. While Figure 6.2 shows increasing reflectance values for wavelengths greater than 3 μm, they are still lower than predicted theoretically. However, the trend is consistent for both theoretical and experimental results for wavelength values greater than 3 μm. The theoretical results represent reflectance values that decrease in the wavelength range between 0.1 and 0.2 μm, which is consistent with Figure 6.2.

The failure to model reflectance in the wavelength range greater than 3 μm may be attributed to some of the assumptions underlying the theory. However, radiation at wavelengths significantly longer than the characteristic dimension of the loops encountered cannot be expected to couple, as suggested by Figure 5.7.

In summary, it is determined that the theoretical model presented here is capable of describing the interaction between electro-magnetic radiation and the simulated gold-black structure in the range of wavelengths between 0.1 and 3 μm.

6.2 Interpretation of Data

In order to fully understand what is being reported in Figures 6.1 and 6.2, one significant simplifying assumption and its impact on the results must be considered. Figure 6.3 is an electrical circuit that represents incident thermal radiation on the left-hand side of the vertical dashed line, and a branch loop represented with a series RLC circuit on the right-hand side of the dashed line. The interface potential difference, v_s, in Figure 6.3 is the same as in Figure 5.5.

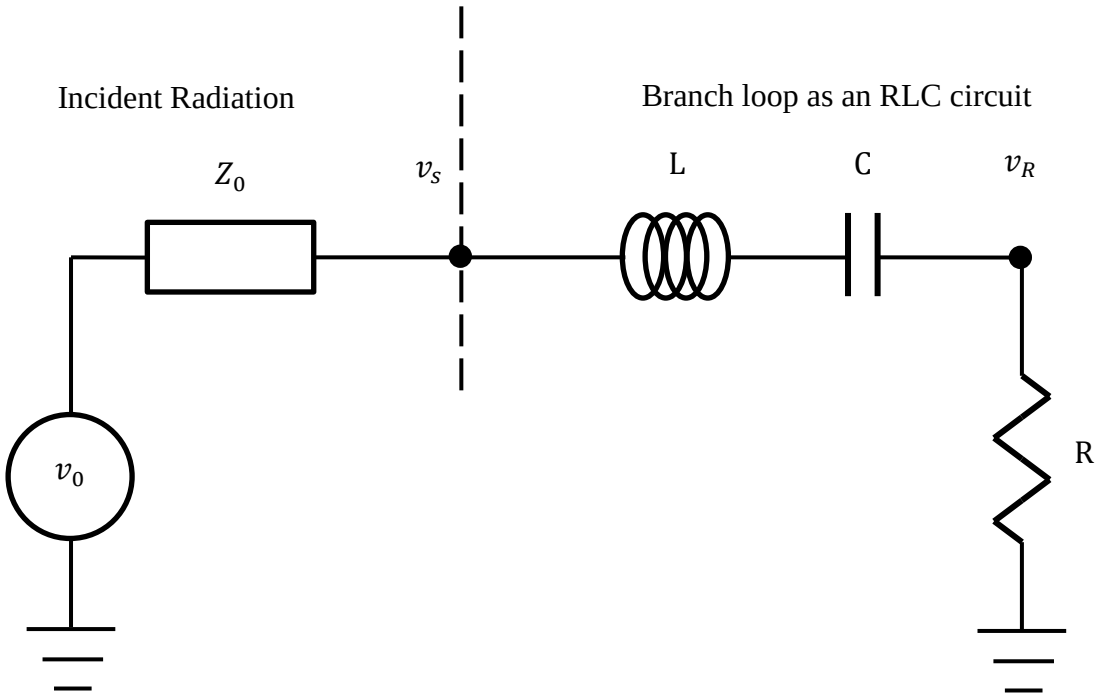

Figure 6.3: RLC circuit with incident radiation.

The reflectivity for this model is given by

$$\rho = \frac{\left(\frac{v_R^2}{R}\right)}{\left(\frac{v_0^2}{Z_0}\right)} , \tag{6.2}$$

where v_0 is the voltage amplitude of the incident radiation and Z_0 is the impedance of free space.

The model proposed in Chapter 5 and experimental results reported in Section 2.3 do not take the impedance of free space into account. As stated in Section 2.3, reference specular reflectance measurements of a polished gold mirror were obtained over the range of wavelengths of interest. All of the measurements where obtained by observing reflectance measurements from a witness sample of pure gold and assuming that its reflectivity was unity. The reflectance measurements shown in Figure 6.2 are calculated according to

$$\rho_{rep} = \frac{P_{ref,gold}}{P_{in}} - \left[1 - \frac{P_{ref,gb}}{P_{in}}\right] , \tag{6.3}$$

where ρ_{rep} are the values for reflectance reported in Figure 6.2, $P_{ref,gold}$ is the reflected power from a pure gold sample, $P_{ref,gb}$ is the power reflected from a gold-black sample, and P_{in} is the incident power. Next, the assumption is made that the incident power is equal to the reflected power from a pure gold sample ($P_{in} = P_{ref,gold}$). After substitution of $P_{ref,gold}$ for P_{in} in Equation 6.3, the equation simplifies to

$$\rho_{rep} = \frac{P_{ref,gb}}{P_{ref,gold}} . \tag{6.4}$$

The theoretical model developed in Chapter 5 and the experimental results in Section 2.3 are both based on this assumption and neglect the effects of the impedance of free space. Figure 6.4 is a schematic representation of the reasoning leading to Equation 6.4.

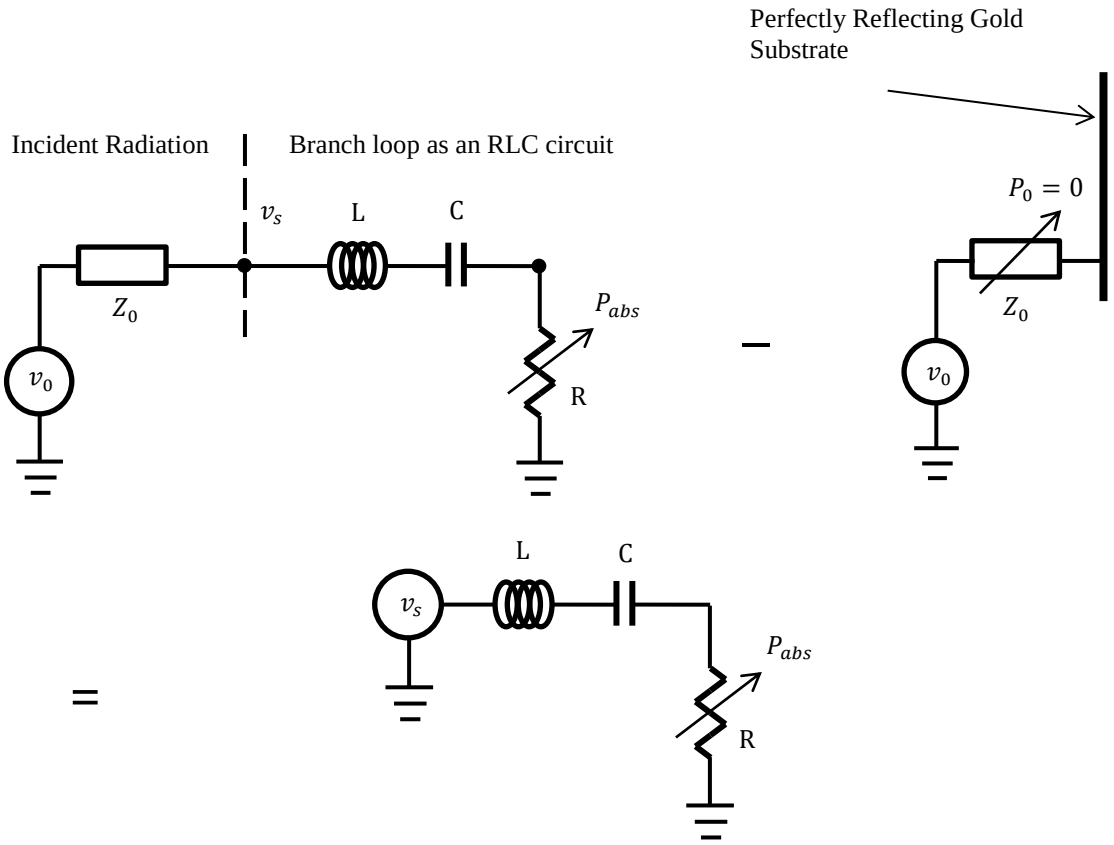

Figure 6.4: Schematic representation of the impact of assuming $P_{in} = P_{ref,gold}$.

The gold substrate is considered to be an essentially perfect reflector of thermal radiation. If gold were indeed a perfect reflector of thermal radiation, the impedance of free space would be zero and thus the voltages at v_0 and v_s would be equal to each other. However, gold is not a perfect reflector of thermal radiation. Bennett and Ashley [1965] report a best case scenario of values of 0.8708 and 0.9942 for the reflectivity of gold of wavelengths of 0.575 and 32 μm, respectively. With a high value for reflectivity, the reflected power by a pure gold substrate will be close to unity. Therefore, the assumption that v_0 and v_s are equal to each other is thought to be an acceptable approximation. On the other hand, if very high accuracy is required, as in the case of earth radiation budget instruments, the assumption that the power

reflected by the gold substrate is equal to the incident power may lead to significant error in the measurement of monochromatic absorptance.

Chapter 7: Conclusions and Recommendations

7.1 Conclusions

The following conclusions can be drawn from the model developed in this thesis describing thermal radiation absorption by gold-black.

1. Gold-black may be successfully simulated using random fractal geometry with an adjustable list of parameters such as those shown in Table 4.1. The values of the list of parameters can be adjusted to simulate the optical behavior of a wide range of gold-black deposits found in the literature.
2. A base model has been successfully constructed to represent the absorption of thermal radiation. The model successfully integrates the random fractal geometry with RLC circuit theory to calculate absorptivity.
3. By defining the geometry for a gold-black deposit and supplying an accompanying theoretical model for absorption, the parameters in Table 4.1 may be adjusted to match specific gold-black deposits in the literature, for example by using parameter estimation.
4. The electrical impedance of gold-black appears to be predominately inductive in the wavelength range of interest.

7.2 Recommendations

The model developed in this thesis provides several avenues for further research.

1. Observation of gold-black growth should be investigated to refine the set of rules developed in this thesis, which are based principally on observations of salt crystals.
2. Optimization of the fractal geometry should be investigated for the development of improved gold-black growth techniques.

3. Coalescing of small gold droplets into larger particles such as sphere like “blobs” should be incorporated into the simulation during early growth.
4. A model of the transport of thermal energy through the gold-black structure to an underlying substrate should be developed.
5. Full- and quarter-wavelength absorption should be incorporated into the theoretical model developed in Chapter 5.
6. The theoretical model should be adjusted to simulate absorption at wavelengths greater than 3 μm.
7. Interactions between branch loops should be developed and incorporated into the theoretical model developed in Chapter 5.
8. For long wavelengths, the absorption and reflection of the underlying material should be incorporated into the theoretical model developed in Chapter 5.
9. Formal parameter estimation methods should be applied in order to match specific gold-black deposits in the literature.
10. The impedance of free space should be incorporated into the theoretical model and compared with reflectance measurements based and the same principle.

References

Becker, W., R. Fettig, A. Gaymann, and W. Ruppel, "Black Gold Deposits as Absorbers for Far Infrared Radiation" *Phys. Status Solidi B,* Vol. B 194, pp. 241-255, 1996.

Becker, W., R. Fettig, and W. Ruppel, "Optical and electrical properties of black gold layers in the far infrared" *Infrared Physics & Technolog.,* Vol. 40 pp. 431-445, April 1999.

Bennett, Jean M. and E. J. Ashley, "Infrared Reflectance and Emittance of Silver and Gold Evaporated in Ultrahigh Vacuum", *Applied Optics,* Vol. 4, No. 2 1965.

Bunde, Armin., *Fractals and Disordered Systems.* Springer-Verlag, Berlin, 1991.

Chen, Shuping, Shuting Yao, and Fushou Xie "Analysis of Thermal Conductivity of Frost on Cryogenic Finned-tube Vaporizer Using Fractal Method", *Energy and power Engineering,* Vol. 5 No. 4B, 2013, pp. 109-115.

Cohen, Nathan., "Fractal Antenna Applications in Wireless Telecommunications", *Proceedings of the Electronics Industries Forum of New England,* 1997, pp 43-49.

Gross, Frank B., *Frontiers in Antennas: Next Generation Design & Engineering,* McGraw-Hill Book Company, Inc., New York, 2011.

Harris, Louis and John K. Beasley, "The Infrared Properties of Gold Smoke Deposits" *Journal of the Optical Society of America,*Vol. 42, pp. 134-140, Feb 1952.

Harris, Louis and Kermit F. Cuff, "Reflectance of Goldblack Deposits, and Some Other Materials of Low Reflectance from 254mμ to 1100mμ. The Scattering-Unit-Size in Goldblack Deposits" *Journal of The Optical Society of America,* Vol. 46, pp 160-163, Mar 1956.

IBM, 2011, Fractal Geometry, http://www-03.ibm.com/ibm/history/ibm100/us/en/icons/fractal/.

Ilias, S., P. Topart, C. Larouche, P. Beaupré, D. Gay, C. Proulx, T. Pope, C. Alain "Deposition and Characterization of gold-black coatings for thermal infrared detectors" *SPIE,* Vol. 7750, 2010.

Jackson, J. D. *Classical Electrodynamics,* Wiley, New York, 1975, p. 80.

Jefco, Inc., Magic Salt Crystal Garden, www.mrsstewart.com.

Kaye, Brian H. *A Random Walk Through Fractal Dimensions,* 2nd ed. Weinheim. VCH, 1994.

Liu, S. H., "Fractal Model for the ac Response of a Rough Interface", *The American Physical Society*, Vol. 55 No 5., 1984.

Mandelbrot, Benoit B., *The Fractal Geometry of Nature,* Ed.1983, Updated and Augm. Ed. New York, 1983.

McKenzie, D. R., "Selective nature of gold-black deposits" *Optical Society of America,* Vol. 66, No. 3, March 1976.

NASA, 2015, Clouds and the Earth's Radiant Energy System, http://ceres.larc.nasa.gov/.

NASA, 2011, What is the Earth's Radiation Budget?, http://science-edu.larc.nasa.gov/EDDOCS/whatis.html

Neli, Roberto R., Ioshiaki Doi, Jose A. Diniz, and Jacobus W. Swart, "Development of process for far infrared sensor fabrication" *Sensors and Actuators,* Vol. 132, pp. 400-406, May 2006.

Nelms, N. and J. Dowson, "Goldblack coating for thermal infrared detectors" *Sensors and Actuators A*, Vol. 120, pp. 403-407, Jan 2005.

Panjwani, Deep., Mehmet Yesiltas, Janardan Nath, D. E. Maukonen, Imen Rezadad, Evan M. Smith, R. E. Peale, Carol Hirschmugl, Julia Sedlmair, Ralf Wehlitz, Miriam Unger, Glenn Boreman, "Patterning of oxide-hardened gold-black by photolithography and metal lift-off" *Infrared Physics & Technology,* Vol. 62, pp. 94-99, 2014.

Panjwani, Deep., Mehmet Yesiltas, Simranjit Singh, Enrique Del Barco, R. E. Peale, Carol Hirschmugl, Julia Sedlemair, "Stencil Lithography of gold-black IR absorption coatings" *Infrared Physics & Technology,* Vol. 66, pp. 1-5, 2014.

Peitgen, Heinz-Otto, H. Jürgens, and D. Saupe. *Chaos and Fractals: New Frontiers of Science,* Springer, New York, 2004.

Pfund, A. H., "Bismuth Black and Its Applications" *Review of Scientific Instruments,* Vol. 1 pp. 397, 1930.

Priestley, Kory James, **Use of First-Principle Numerical Models to Enhance the Understanding of the Operational Analysis of Space-Based Earth Radiation Budget Instruments**, Doctoral of Philosophy Dissertation, Department of Mechanical Engineering, Virginia Polytechnic Institute and State University, Blacksburg VA, 1997.

Rosa, E.B., "The Self and Mutual Inductances of Linear Conductors", *Bulletin of the Bureau of Standards,* 1908, 4 (2): 301–344.

Schroeder, M. R., *Fractals, Chaos, Power Laws: Minutes from an Infinite Paradise.* Dover Publications, Dover, N.Y., 2009.

Strogatz, Steven H., *Nonlinear Dynamics and Chaos,* Westview Press, Philadelphia, 2015.

Stratton, J. A., *Electromagnetic Theory*, McGraw-Hill Book Company, Inc., New York, 1941, pp. 268-278.

Witten, T. A and L. M. Sander, "Diffusion-Limited Aggregation, a Kinetic Critical Phenomenon" *The American Physical Society,* Vol 47 No 19, 1981.

Appendix A: Matlab Program

```
%%%%%%% run_experiment %%%%%%%%%%%%%%%%%%%%%%%%%%%%%%%
%%%%%%%%%%%%%%%%%%%%%%%%%%%%%%%%%%%%%%%%%%%%%%%
%%%%%
% This program is a part of the thesis by Brendan Quinlan (A model for
% absorption of thermal radiation by gold-black).  This model simulates gold-
% black as fractal geometry. This program provides the user with an image
% of the simulated geometry and the number of branches and connections.
%%%%%%%%%%%%%%%%%%%%%%%%%%%%%%%%%%%%%%%%%%%%%%%
%%%%%

%%%%%%%%%%%%%%%%%%%%%%%%%%%%%%%%%%%%%%%%%%%%%%%
%%%%%
%%%%%%%%%%% Instructions to run the program %%%%%%%
% In order to run this program copy the text under run_exeriment into a
% new script file.  Save the file as run_experiment.  Open
% another script file and copy the text under calc_dist_3d and
% save the other script file as calc_dist_3d.  Type
% run_experiment('3d') into the command window and press enter.
% Note if g is set to 10 or more computational time may take
% 30 to 40 minutes as 2015
%%%%%%%%%%%%%%%%%%%%%%%%%%%%%%%%%%%%%%%%%%%%%%%
%%%%%


%   Main function to generate gold-black simulation
function run_experiment(inArg)

tic
    warning off

    if nargin == 0
        inArg = '2d';
    end

    addpath(genpath('.'));

    close all;
    clc

    params = get_params;

%     Choose to create 2d or 3d geometry by typing run_experiment('2d') or
%     run_experiment('3d') into the command window
    inArg = lower(inArg);
```

```
   if strcmp(inArg, '2d')
      params.dim = 1;
   elseif strcmp(inArg, '3d')
      params.dim = 0;
   end

%     Initializing queue stack
   queue = {};

%     Initialize tracking parameters
      global branch_track_count_mat;
      global branch_track_mat;
      global branch_tracking_mat;
      global branch_track;
      global branch_track_count;

      branch_track_count_mat = [];
      branch_track_mat = [-1];
      branch_tracking_mat = [];
      branch_track = 1;
      branch_track_count = 0;

%     generating nucleation sites for 2d or 3d geometry
   if params.dim == 1

%        2d geometry
       for ind = 1:params.numStartPos
          queue{end + 1} = {[0, params.compression*(rand-0.5)], [], 1};
       end

   else
%        3d geometry
       for ind = 1:params.numStartPos
          queue{end + 1} = {[params.compression*(rand-0.5), params.compression*(rand-0.5),0],
[], 0};
       end
   end

%     initializing connections stack
   connections = {};

      gen_track_count_mat = [];
      gen_track_mat = [1];
      connection_tracking_mat = [];
      gen_track = 1;
      gen_track_count = 0;
```

```
%    iteration counter
   itr = -1;

   while ~isempty(queue)
      itr = itr + 1;

%        using dequeue function to delete old node locations and store
%        into node stack
      [node, queue] = dequeue(queue);

%        intersection function checks if an intersection has occurred between
%        two branches and connects the branches and terminates growth or
%        terminates growth for one and allows growth to continue for the other

      [isInt, pos] = is_intersection(node, connections, params);
      if isInt
%           fprintf('is intersection\n');
         %ADD CODE to use pos
%             Adds sets of nodes that create branches to the connections stack
         if length(pos) > 3
            pos = pos(1:end-1);
         else
            fprintf('missing distance\n');

         end
         node{1} = pos;


         if gen_track ~= node{3}
            gen_track = node{3};
            gen_track_mat(end + 1) = node{3};
            gen_track_count_mat(end + 1) = gen_track_count;
            gen_track_count = 1;

         elseif gen_track == node{3}
            gen_track_count = gen_track_count + 1;

         end

         if itr > 0
            connections{end + 1} = node;
         end

         continue;
      end
```

```
%       adds_new_pts function adds new node locations to the queue
      queue = add_new_pts(queue, node, params);

%       Adds sets of nodes that create branches to the connections stack
      if itr > 0
         connections{end + 1} = node;
      end

   end
   branch_track_count_mat(end + 1) = branch_track_count;
%
   branch_track_mat = branch_track_mat + 1;
   branch_tracking_mat = [branch_track_mat', branch_track_count_mat'];
   branch_tracking_mat

   gen_track_count_mat(end + 1) = gen_track_count;
%    gen_track_mat = gen_track_mat - 1;
   connection_tracking_mat = [gen_track_mat', gen_track_count_mat'];
   connection_tracking_mat

%    plots connections stack for either 2d or 3d to create geometry

   figure(1);

   fprintf('ready to plot\n');

   hold on;

   for ind = 1:length(connections)
      if length(connections{ind}) > 1
         pos = [connections{ind}{1}; connections{ind}{2}];
         gen = connections{ind}{3};

         if params.dim == 1
%             2d plot
            plot(pos(:, 1), pos(:, 2), 'b');
            axis([-params.axisView params.axisView 0 params.axisView]);
         else
            if gen <= 10
%             3d plot
%
            plot3(pos(:, 1), pos(:, 2),pos(:, 3),'LineWidth',10.0/(gen+1), 'Color', [1-
(gen/(params.g)) 1-(gen/(params.g)) 1-(gen/(params.g))]);
```

```
                axis([-params.axisViewXY params.axisViewXY -params.axisViewXY
params.axisViewXY 0 params.axisViewZ]);
                else
                    continue
                end
            end
        end
    end

    whitebg(figure(1), [0 0 0]) %set(growthPlot,'BackgroundColor',[0 0 0]);
    hold off;


    toc

end

%%%%%%%%%%%%%%%%%%% Important
%%%%%%%%%%%%%%%%%%%%%%%%%%%%%%%%%%%%%
%%%%%%%%%%%%%%%%%%%%%%%%%%%%%%%%%%%%%%%%%%%%%%
%%%%%%%%%%%%%%%%%%%%%
% parameter function defines the critical parameters used to adjust
% gold-black growth
%%%%%%%%%%%%%%%%%%%%%%%%%%%%%%%%%%%%%%%%%%%%%%
%%%%%%%%%%%%%%%%%%%%%
function params = get_params

    %2d parameters
%     params.const = 0.9;
%     params.sd = 0.1;
%     params.start = 1.2;
%     params.axisView = 10;
%     params.g = 10;
%     params.compression = 8;
%     params.numStartPos = 10;
%     params.branch_percentage = .7;
%     params.branch_termination_percentage = 0.7;
%     params.z_std_dev = 0.1;

    %3d parameters
    params.angle = 10; %angle is in degrees
    params.const = 0.93;
    params.sd = sqrt(pi)*sin(params.angle*(pi/180))/sqrt(2);
    params.start = 3.3;
    params.axisViewXY = 10;
    params.axisViewZ = 30;
```

```
    params.g = 5;
    params.compression = 10;
    params.numStartPos = 6;
    params.branch_percentage = .7;
    params.z_std_dev = 0.1;


end


function queue = add_new_pts(queue, node, params)

    global branch_track_count_mat;
    global branch_track_mat;
    global branch_track;
    global branch_track_count;

    prevPos = node{1}; %strating position for each node
    gen = node{3};
    %**************************************

    if gen >= params.g
        return;
    end

%     generating either two-branch pattern or three-branch pattern
    value2 = rand;
    if value2 < params.branch_percentage
        numPts = 2;
    else
        numPts = 3;
    end

    if params.dim == 1
        for ind = 1:numPts

%             two dimensional coordinates
            newx = prevPos(1) + params.start*(params.const^gen)*(normrnd(0,params.sd));
            newy = prevPos(2) + params.start*(params.const^gen);
            newPos = [newx, newy];

            queue = enqueue(queue, {newPos, prevPos, gen + 1});

        end
    else
        for ind = 1:numPts
```

```
        % generating normally dist random numbers for x y and z
        rand_x = params.start*(params.const^gen)*(normrnd(0,params.sd));
        rand_y = params.start*(params.const^gen)*(normrnd(0,params.sd));

        rand_z =
normrnd(params.start*(params.const^gen)*cos(params.angle*(pi/180)),params.z_std_dev);

%           adding to previous position
        newx = prevPos(1) + (rand_x);
        newy = prevPos(2) + (rand_y);
        newz = prevPos(3) + rand_z;
        newPos = [newx, newy, newz];

        queue = enqueue(queue, {newPos, prevPos, gen + 1});

%           tracking number of branches
        if branch_track ~= node{3}
           branch_track = node{3};
           branch_track_mat(end + 1) = node{3};
           branch_track_count_mat(end + 1) = branch_track_count;
           branch_track_count = 1;

        elseif branch_track == node{3}
           branch_track_count = branch_track_count + 1;

        end

      end
   end
end

function [boolVal, pos] = is_intersection(node, connections, params)

   boolVal = false;
   pos = [];
   if isempty(node{2})
      return;
   end
   ncon = [node{2}, node{1}];
   gen_node = node{3};

%    converting connections cell array to a matrix for filtering
%    in calc_dist_3d function
   A = cellfun(@(arg) [arg{1:2}], connections, 'UniformOutput', false);
   lengths = cellfun(@(arg) length(arg), A);
```

```
    A = A(lengths > 3);

    if isempty(A)
        return;
    end
    %try and catch statements are just to help troubleshoot. could take them out
    %and just leave [pos, boolVal] = calc_dist_3d(cell2mat(A'), ncon);
    %but decided to leave in
    try
%       sending to calc_dist_3d function located in another script in the
%       same directory
    [pos, boolVal] = calc_dist_3d(cell2mat(A'), ncon, gen_node, params);
    catch
%       debug statements
        fprintf('I hit a stop\n');
        stophere = 1;
    end

end

function [node, queue] = dequeue(queue)
    node = queue{1};
    queue(1) = [];
end

function queue = enqueue(queue, node)
    queue{end + 1} = node;
end
```

```
%%%%% calc_dist_3d %%%%%%%%%%%%%%


function [pos, isconnection] = calc_dist_3d(A, New_connection, gen_node, params)



%%%%%%%%%%%%%%%%%%%%%%%%%%%%%%%%%%%%%%%%%%%%%%
%%%%%%%%%%%%%%%%%%%%
    %%%%%%%%%%%%%%%%%%%%%%%%    if 3d go from here
%%%%%%%%%%%%%%

%%%%%%%%%%%%%%%%%%%%%%%%%%%%%%%%%%%%%%%%%%%%%%
%%%%%%%%%%%%%%%%%%%%

    isconnection = false;
    pos = [];
    closestValue_total = [1000,1000,1000,1000];
    range = 2; %sets the
    two_diameters = (params.start*params.const^gen_node)*(1/10);

%     Filtering far away branches

%%%%%%%%%%%%%%%%%%%%%%%%%%%%%%%%%%%%%%%%%%%%%%
%%%%%%%%%%%%%%%%%%%%
    if isempty(A)
%         S = 'No connections';
%         disp(S)
    else
        A(range + max(New_connection(1),New_connection(4)) < A(:, 4) |
min(New_connection(1),New_connection(4) + (-range)) > A(:, 4), :) = [];
    end

    if isempty(A)
%         S = 'No connections';
%         disp(S)
    else
        A(range + max(New_connection(2),New_connection(5)) < A(:, 5) |
min(New_connection(2),New_connection(5) + (-range)) > A(:, 5), :) = [];
    end

    if isempty(A)
%         S = 'No connections';
%         disp(S)
```

```
   else
      A(range + max(New_connection(3),New_connection(6)) < A(:, 6) |
min(New_connection(3),New_connection(6) + (-range)) > A(:, 6), :) = [];
   end

   if isempty(A)
%        S = 'No connections';
%        disp(S)
   else
      A(range + max(New_connection(1),New_connection(4)) < A(:, 1) |
min(New_connection(1),New_connection(4) + (-range)) > A(:, 1), :) = [];
   end

   if isempty(A)
%        S = 'No connections';
%        disp(S)
   else
      A(range + max(New_connection(2),New_connection(5)) < A(:, 2) |
min(New_connection(2),New_connection(5) + (-range)) > A(:, 2), :) = [];
   end

   if isempty(A)
%        S = 'No connections';
%        disp(S)
   else
      A(range + max(New_connection(3),New_connection(6)) < A(:, 3) |
min(New_connection(3),New_connection(6) + (-range)) > A(:, 3), :) = [];
   end

   if isempty(A)
%        S = 'No connections';
%        disp(S)
   else
      A((New_connection(1) == A(:, 4)) & (New_connection(2) == A(:, 5)) &
(New_connection(3) == A(:, 6)), :) = [];
   end

   if isempty(A)
%        S = 'No connections';
%        disp(S)
   else
      isconnection = true;
%%%%%%%%%%%%%%%%%%%%%%%%%%%%%%%%%%%%%%%%%%%%%%%%%%%%%%%%%%%%%%%%%%%%%%%%
      for j = 1:size(A,1)
```

```
Q = [A(j,1),A(j,2),A(j,3)];
P = [A(j,4),A(j,5),A(j,6)];

R = [New_connection(1),New_connection(2),New_connection(3)];
S = [New_connection(4),New_connection(5),New_connection(6)];
divisions = 15;

xpointmat = [];
ypointmat = [];
zpointmat = [];
distancemat = [];
start_distance_mat = [];
end_distance_mat = [];


N = null(P-Q);

x = linspace(R(1),S(1),divisions);
y = linspace(R(2),S(2),divisions);
z = linspace(R(3),S(3),divisions);

xyz = [x', y', z'];

for k = 1:divisions

    u = (Q-P)'\((xyz(k,:) - (xyz(k,:)*N)*N') - P)';

    point = P + u*(Q-P);

    start_distance = sqrt((xyz(k,1)-P(1))^2+(xyz(k,2)-P(2))^2+(xyz(k,3)-P(3))^2);
    end_distance = sqrt((xyz(k,1)-Q(1))^2+(xyz(k,2)-Q(2))^2+(xyz(k,3)-Q(3))^2);

    start_distance_mat(end + 1) = start_distance;
    end_distance_mat(end + 1) = end_distance;


    if max(P(1),Q(1)) < point(1) || point(1) < min(P(1),Q(1))
        continue
    elseif max(P(2),Q(2)) < point(2) || point(2) < min(P(2),Q(2))
        continue
    elseif max(P(3),Q(3)) < point(3) || point(3) < min(P(3),Q(3))
        continue
    else
        xpointmat(end + 1) = point(1);
        ypointmat(end + 1) = point(2);
        zpointmat(end + 1) = point(3);
```

```
        distance = norm(P + u*(Q-P) - xyz(k,:));

        distancemat(end + 1) = distance;

      end

   end

   xyzpointmat = [xpointmat', ypointmat', zpointmat',distancemat'];


   min_at_start = min(start_distance_mat(1,:));
min_at_end = min(end_distance_mat(1,:));

if isempty(xyzpointmat)
   if min_at_start > min_at_end

      q = Q;
      q(end + 1) = min_at_end;
      closestValue = q;
   else
      p = P;
      p(end + 1) = min_at_start;
      closestValue = p;
   end
else

   closestValues = min(xyzpointmat(:,4));

   if closestValues > min(min_at_start,min_at_end)

      if min_at_start > min_at_end

         q = Q;
      q(end + 1) = min_at_end;
      closestValue = q;
      else
         p = P;
      p(end + 1) = min_at_start;
      closestValue = p;
      end
   else
      [c index] = min(xyzpointmat(:,4));
      closestValue = xyzpointmat(index,:); % Finds first one only!
   end
```

```
        end

        if closestValue_total(1,4) > closestValue(1,4)
            closestValue_total = closestValue;
        end

            pos = closestValue_total;

        end
        if closestValue_total(1,4) > two_diameters
            isconnection = false;
        end
    end

end
```

Appendix B: Mathematica Program

```
(*10 degree branch angle sim 5*)
branch = List[17, 38, 85, 172, 331, 619, 1062, 1537, 2026, 2704];

branchFuncVars = {a, b, cc, dd} /.
  FindFit[branch, a x^3 + b x^2 + cc x + dd, {a, b, cc, dd}, x]

(*full half and quarter wavelength adjuster*)
jj = 2;

(*wavelength range*)
 λmin = 0.05;
 λmax = 100;

(*point resolution for plotting*)
PointResolution = 0.01;

(*steady state transfer function for RLC circuit (Vr/Vs)*)
H[f_, L_, R_,
  c_] := (Sqrt[1 + ((1/(2 \[Pi]*f*c*R)) - ((2 π*f*L)/R))^2])^-1
(*Resistor inductor and capacitor values for RLC circuit*)
R[ρ]_, l_, Ac_] := ρ*l/Ac;
c[ϵ_, d_, l_,
   dis_] := (π*ϵ*
     l)/(Log[(dis/(d)) + Sqrt[(dis^2/(d^2)) - 1]]);
L [l_, d_, μ_,
   dis_] := (μ*l/π) Log[(dis/(d)) + Sqrt[(dis^2/(d^2)) - 1]];

(*function to calculate the average branch length for each generation*)


branchLength [g_] := ((3.3*10^-6)*0.93^g);
(*extrapolation function that gives the number of branches for each \
generation*)
branchFunc[
   gen_] := (branchFuncVars[[1]]*(gen)^3 +
    branchFuncVars[[2]]*(gen)^2 + branchFuncVars[[3]]*gen +
    branchFuncVars[[4]]);

(*inituilizing a lists for wavelength and power totaling list*)
PrtotalallfullhalfquarterList =
  Table[0*i, {i, ( λmax - λmin)/PointResolution}];
waveTable =
  Table[λt, {λt, λmin, λmax,
    PointResolution}];
```

```
(*for loop to analyze full quarter and half wavelengths*)
For[j = 1, j <= 1, j++,

 (*debug statement
 Print["I Came Here"];
 *)

 (*initialize power absorbed total list for each wavelength generated \
in wavetable*)
 PrtotalallList = List[];

 i = 1;

 (*full half or quarter wavelength multiplier*)
 aa = 1/jj;

 (*loop to analyze each wavelength*)
 For[i = 1, i <= ( λmax - λmin)/PointResolution, i++,
  g = 46;
  gPerm = g;
  n = 0;
  Prtotalall = List[];
  PrFrac = 1;

  (*loop to analyze each generation*)
  While[n < g,

   ϵ = 8.854*10^-12;
   μ = 1.2566*10^-6;
   ρ = 2.44*10^-8;
   l = waveTable[[i]]*10^-6/aa;
   d = branchLength [g]/10;
   dis = 2*branchLength [g]/10;
   Ac = 0.25*π*d^2;
   λ = waveTable[[i]]*10^-6;
   f = 2.9979*10^8/λ;

   (*equivalent values calculated*)
   ris = 2*R[ρ, l, Ac];
   cap = (1/c[ϵ, d, l, dis] +
      1/c[ϵ, d, l, dis])^-1;
   ind = 2*L[l, d, μ, dis];

   (*voltage over the resistor (assuming Vs=
   1) and power dissipated across the resistor*)
```

```
    vr = H[f, ind, ris, cap];
    Pr = (vr^2/ris);

    (*logic statement to invert the multiplier*)
    If[(l/branchLength[g]) <= 1,
     (*total power for each generation*)
     Prtotal = Pr*(l/branchLength[g])*((branchFunc[g]/(1)));
     Prtotalall = Append[Prtotalall, PrFrac*Prtotal];
     (*calculating the fraction of power that penitrates down into \
each layer*)
     PrFracTotal = Total[Prtotalall];
     PrFrac = 1 - (PrFracTotal);
     ,
     Prtotal = Pr*(l/branchLength[g])^-1*((branchFunc[g]/(1)));
     Prtotalall = Append[Prtotalall, PrFrac*Prtotal];
     PrFracTotal = Total[Prtotalall];
     PrFrac = 1 - (PrFracTotal);
     ]
    g = g - 1;

    ]
   Total[Prtotalall];

   PrtotalallList = Append[PrtotalallList, Total[Prtotalall]];

  ]
 jj = jj + 2;
PrtotalallfullhalfquarterList =
 PrtotalallList + PrtotalallfullhalfquarterList

]

PrtotalallfullhalfquarterList;

ListLogLinearPlot[(PrtotalallfullhalfquarterList),
 DataRange -> { λmin, λmax},
 PlotRange -> {{ λmin, λmax}, {0, 1}},
 PlotStyle -> {PointSize[0.015], Blue, Thick},
 AxesOrigin -> {λmin, 0},
 AxesLabel -> {"λ (μm)", "α"},
 AxesStyle -> Directive[Black],
 LabelStyle -> Directive[Black, Bold]]

ListLogLinearPlot[100 (1 - (PrtotalallfullhalfquarterList)),
 DataRange -> { λmin, λmax},
 PlotRange -> {{ λmin, λmax}, {0, 10}},
```

```
 PlotStyle -> {PointSize[0.015], Blue, Thick},
 Frame -> True,
 FrameStyle -> Directive[Black],
 FrameLabel -> {"λ (μm)", "ρ (%)"},
 LabelStyle -> Directive[Black, Bold]]

plot1 = Plot[branchFunc[x], {x, 0, 20},
   PlotStyle -> {Blue, Thick},
   AxesOrigin -> {0, 0},
   AxesLabel -> {"g", "B"},
   AxesStyle -> Directive[Black],
   LabelStyle -> Directive[Black, Bold]];

plot2 = ListPlot[branch, PlotStyle -> {PointSize[0.015], Red},
   AxesOrigin -> {0, 0},
   AxesLabel -> {"g", "B"},
   AxesStyle -> Directive[Black],
   LabelStyle -> Directive[Black, Bold]];

Show[{plot1, plot2}]
```